

# A Deep Learning Earth System Model for Efficient Simulation of the Observed Climate

Nathaniel Cresswell-Clay<sup>1</sup>, Bowen Liu<sup>1,2</sup>, Dale R. Durran<sup>1</sup>, Zihui Liu<sup>1</sup>,  
Zachary I. Espinosa<sup>1</sup>, Raul A. Moreno<sup>1</sup>, Matthias Karlbauer<sup>3</sup>

<sup>1</sup>University of Washington  
<sup>2</sup>Institute of Atmospheric Physics, CAS  
<sup>3</sup>University of Tübingen

## Key Points:

- The coupled atmosphere-ocean Deep Learning Earth System Model (*DLESyM*) simulates 1,000 years of equilibrium climate in less than 12 hours.
- While only trained to optimize MSE over 24 hours in the atmosphere, *DLESyM* produces realistic climatology and interannual variability.
- The equilibrium climate simulated by *DLESyM* has high fidelity to observed climate, competitive with state-of-the-art CMIP6 models.

**Abstract**

A key challenge for computationally intensive state-of-the-art Earth System models is to distinguish global warming signals from interannual variability. Here we introduce *DLESyM*, a parsimonious deep learning model that accurately simulates the Earth’s current climate over 1000-year periods with no smoothing or drift. *DLESyM* simulations equal or exceed key metrics of seasonal and interannual variability—such as tropical cyclone genesis over the range of observed intensities, the cycle of the Indian Summer monsoon, and the climatology of mid-latitude blocking events—when compared to historical simulations from four leading models from the 6th Climate Model Intercomparison Project. *DLESyM*, trained on both historical reanalysis data and satellite observations, is an accurate, highly efficient model of the coupled Earth system, empowering long-range sub-seasonal and seasonal forecasts while using a fraction of the energy and computational time required by traditional models.

**Plain Language Summary**

Machine learning (ML) based atmosphere models have recently demonstrated the ability to accurately predict weather over 10 days, and have proven superior to operational weather prediction systems based on conventional numerical methods. Many of these ML weather models, however, fail to recreate our atmosphere over longer simulations. Predicted states tend to become overly smooth, physically unrealistic, or entirely unstable. In this work we build on canonical understanding of Earth System variability by coupling an ML weather model to an ML-based model of the sea-surface. This coupling results in an Earth System model that can freely evolve without unrealistic behavior. The model is called Deep Learning Earth SYstem Model or *DLESyM*. While parsimonious in its design, *DLESyM* is capable of producing thousands of years of realistic atmosphere and ocean states including seasonal cycles, spontaneous tropical cyclones, strong winter storms, and even interannual variability. Our results are compared to those of conventional numerical Earth System models from CMIP6 demonstrating *DLESyM*’s competitive fidelity to the internal variability of the Earth System. Crucially the computational cost of running *DLESyM* is significantly less compared to traditional models, making it a powerful yet affordable tool for the study of weather and climate variability.

**1 Introduction**

Accurately simulating seasonal and interannual variability in Earth System models is essential for improving sub-seasonal and seasonal forecasting (involving lead times from 2 weeks to several months) and for distinguishing global warming signals from natural variability. Recently developed atmosphere-only deep learning (DL) models provide good deterministic global weather forecasts out to about 10 days, but generally become unstable or exhibit low skill during multi-month simulations (Karl Bauer et al., 2024; Bi et al., 2023; Lam et al., 2023). In this work, we present a deep learning model, which couples the atmosphere with the ocean. Our model can realistically simulate the Earth’s current climate over 1000-year periods with negligible drift. Our performance on key metrics of seasonal and interannual variability—such as tropical cyclone genesis and intensity, and mid-latitude blocking frequency—equals or exceeds that of historical simulations from four computationally intensive models used in the 6th Assessment Report from the Intergovernmental Panel on Climate Change (IPCC). Our model is trained on historical weather data and satellite observations to minimize forecast errors over short periods (24-h in the atmosphere and 8 days in the asynchronously coupled ocean), yet the correct seasonal and interannual variability emerges in free-running simulations. This impressive ability to learn the current climate using short-period training data sidesteps concerns about the lack of appropriate long-period datasets to train purpose-built DL

models for seasonal forecasting (de Burgh-Day & Leeuwenburg, 2023). Our model is an accurate, highly efficient model of the full Earth System, bridging the gap between traditional weather and climate modeling.

Multi-year simulations with deterministic DL numerical weather prediction models have been achieved by appropriately incorporating the sea-surface temperature (SST) as lower boundary conditions. Specifying climatological SST as external forcing can improve the fidelity of some DL and DL-hybrid atmospheric models over decadal rollouts (Watt-Meyer et al., 2023; Kochkov et al., 2023) and transient SST forcing can occasion realistic atmospheric trends (Watt-Meyer et al., 2024). Hybrid coupled modeling in which one component of the Earth System, represented with an DL-based model is coupled to another physics-based component model have demonstrated that the two approaches can work well together, creating stable representations of the Earth System (Arcomano et al., 2023; Clark et al., 2024). As an initial step with a fully DL coupled atmosphere-ocean model (C. Wang et al., 2024) were able to approximate oceanic signatures of El Niño and equatorial waves, remaining stable for up to 6 months.

Traditional numerical models of the coupled Earth System have proved a powerful tool for scientists, facilitating the study of atmosphere-ocean interactions and feedbacks (Woollings et al., 2012; Herceg-Bulić & Kucharski, 2014; Gupta & England, 2007). Their stability over long simulations and ensembling capability has also proven useful in the study of internal climate variability (Mann et al., 2014; Marotzke & Forster, 2015). Indeed, coordinated experiments with state-of-the-art (SOTA) Earth System models through the Coupled Model Intercomparison Project (CMIP), have become one of the foundational elements of climate science (Eyring et al., 2016). These models, however, require enormous computational resources available only at large national and international centers. This large overhead constrains the use of SOTA climate models and encourages the development of novel methods that increase accessibility of high fidelity models.

Our Deep Learning Earth SYstem Model (*DLESyM*) couples a deep learning weather prediction model (DLWP) (Karl Bauer et al., 2024) with a deep learning ocean model (DLOM). We examine the performance and climatology of *DLESyM* over 100- and 1000-year iterative rollouts and find its fidelity to many aspects of the current climate system comparable or even superior to several leading CMIP6 models. Our simulations do not receive anthropogenic forcing and so express an equilibrium climate. Despite being an autoregressive model with no generative components, *DLESyM* forecasts continue to generate sharply defined weather patterns over 730,000-step simulations. As in SOTA CMIP6 Earth System models, the coupling between the atmosphere and the ocean in *DLESyM* is asynchronous, with 6-hour time resolution in the atmosphere and 2-day resolution in the ocean. In comparison to the most successful medium-range ML forecast models (Bi et al., 2023; Lam et al., 2023; K. Chen et al., 2023; L. Chen et al., 2023; Lang et al., 2024), we adopt a much more parsimonious approach using an order of magnitude fewer prognostic variables at each grid point: 9 for the atmosphere and just SST for the ocean. Precipitation is not simulated directly as part of the autoregressive rollout, but rather diagnosed from the forecast fields with a separate DL module. Our training data includes fields from the ERA5 reanalysis (Hersbach et al., 2020), but in contrast to previous models, we extend our set of prognostic fields to include outgoing long-wave radiation (OLR) to train on direct observations from the International Satellite Cloud Climatology Project (ISCCP) (Young et al., 2018).

In this study, we will first outline important aspects of our model design, including an overview of training data. Then, we discuss the stability and fidelity of *DLESyM* over millennial simulations. Afterwards, we expand our assessment of model fidelity by examining its representation of tropical cyclones and extratropical modes of variability. We also present the performance of the model in simulating the Indian Summer Monsoon (ISM). Finally we discuss El Niño Southern Oscillation (ENSO) teleconnections and variability within *DLESyM* simulations.

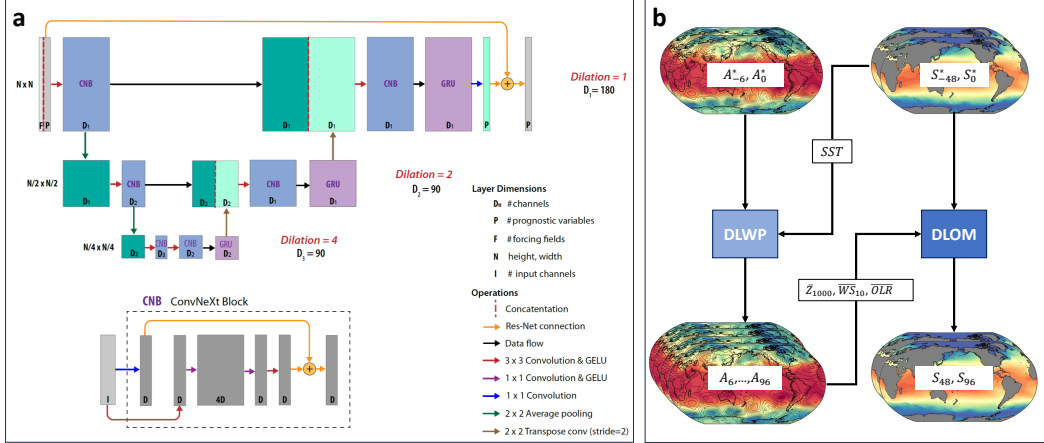


**Figure 1. Architecture and coupling of DLESyM.** (a) Schematic representation of the DLWP module as a sequence of operations on layers (see legend). U-net levels are labeled by their channel depth, with  $D_1 = 180$  and  $D_2 = D_3 = 90$  being associated with the first convolutions in each level. Each ConvNeXt block (blue) is replaced by the layers and operations shown in the inset labeled CNB, with generic embedding depths  $D$  and  $I$  determined by the channel depth of the input and the labeled value of  $D_n$ . The purple blocks labeled GRU denote convolutional Gated Recurrent Unit layers, which are implemented with  $1 \times 1$  spatial convolutions. Other layers evaluated by the encoder are shown as dark green, while those evaluated by the decoder are shown as light green. (b) DLESyM coupling mechanism. Atmosphere and ocean states are denoted by  $A$  and  $S$ , respectively, with the subscript indicating time in hours with respect to initialization at hour 0. Light blue box represents the atmospheric module (DLWP) while the darker blue represents the ocean (DLOM). Data flow and sequence of calls are given with arrows.

## 2 Model Design

### 2.1 Architecture

DLESyM uses two U-net style convolutional neural networks (Ronneberger et al., 2015) in autoregressive rollouts: one simulating the atmosphere and the other, the ocean. These U-nets build on a series of successful deep learning weather prediction models (Weyn et al., 2020, 2021; Karlbauer et al., 2024). The structure of the atmospheric module is diagrammed in Fig. 1, with the details of the convolutional GRU (Ballas et al., 2015) omitted for simplicity. Unlike the original ConvNeXt block proposed in (Liu et al., 2022), the ConvNeXt block in (Karlbauer et al., 2024) expands the latent-layer depth by a factor of four as part of a spatial convolution with a  $3 \times 3$  kernel. Here we return to an architecture closer to that proposed in (Liu et al., 2022), where the expansion in latent-layer depth is imposed with a  $1 \times 1$  convolutional kernel. The resulting economy in the number of trainable weights allows us to substantially increase the latent-layer depth in each level of the U-net while reducing the total number of trainable parameters from 9.8M to 3.5M without loss of predictive skill.

The ocean module uses the same U-net architecture shown in Fig. 1, except layer depths at each level are reduced to  $D_1 = 90$  and  $D_2 = D_3 = 45$ , and the convolutional GRU is omitted to simplify the coupling algorithm. There are roughly 0.77M trainable parameters in the ocean module. Precipitation is diagnosed with a third U-net model.

This module uses the architecture in Fig. 1 with the GRU’s omitted and basic convolutions in place of the ConvNeXt blocks. The final output is the accumulated precipitation between two input times, rather than an updated model state. The precipitation module uses roughly 1.5M trainable parameters, with latent layer depths  $D_1 = 64$ ,  $D_2 = 128$ ,  $D_3 = 256$ . A more detailed description of the atmosphere, ocean, and precipitation modules is provided in Supporting Information. Full model configurations and weights, as well as prepared initialization data for simulations discussed in this study are published in the associated repository.

## 2.2 Atmosphere-Ocean Coupling

Ocean circulations evolve more slowly than those in the atmosphere so, as in traditional Earth System models, we use a longer time step for our ocean model. The DLOM updates every 4 days; each model step generates SST values at both 48-h and 96-h lead times. In contrast, the atmosphere updates every 12 hours, generating atmospheric fields at both 6-h and 12-h lead times. (See (Karl Bauer et al., 2024) for details about the two-in, two-out time stepping.)

To step the coupled model forward, we proceed in 96-h (4 day) increments. The mechanics of our coupling are illustrated in Fig. 1b. To describe the mechanism of our coupled model, we use  $A$  to represent the atmospheric forecast and  $S$  to represent the oceanic forecast. The star operator,  $*$ , indicates observed values. Subscripts are used to represent time, expressed in hours, relative to the initialization of the simulation with hour 0 being the time at which the forecast is initialized.

First, we call the atmosphere model using past and initial atmospheric states,  $A_{-6}^*$ ,  $A_0^*$  and the initial SST,  $S_0^*$ . This call produces predicted atmospheric states  $A_6$  and  $A_{12}$ . Using these predicted atmospheric states and the same  $S_0^*$ , we call the atmospheric model again. This process is repeated, using the same SST,  $S_0^*$ , throughout, until we obtain a predicted atmosphere through 96 h. The ocean states  $S_{-48}^*$  and  $S_0^*$  are then stepped forward using 10-m windspeed ( $WS_{10}$ ), 1000-hPa height ( $Z_{1000}$ ) and OLR as forcing from the time-averaged atmosphere states  $A_{48} = \text{average}(A_6, \dots, A_{48})$  and  $A_{96} = \text{average}(A_{54}, \dots, A_{96})$  to produce the predicted ocean states  $S_{48}$  and  $S_{96}$ . This completes a full 96-h cycle, which we repeat during iterative rollouts. For a complete list of variables predicted by DLESyM see Supporting Information. Note that the 2-m atmospheric temperature ( $T_{2m}$ ) is not passed to the ocean model to divorce causality from correlation, since the surface temperature over the ocean is primarily forced by the SST, not vice versa.

## 2.3 Training the Deep Learning Earth System Model

While our ocean and atmosphere modules are coupled during inference (section 2.2), they are trained separately. During training, the atmosphere and ocean models learn to incorporate information about the other Earth System component by receiving reanalysis and observed values of the coupled fields. For example our atmosphere model receives ERA5 reanalysis values of SST as input in addition to prognostic variables representing the previous atmospheric state. During inference this SST input is substituted for ocean model output. In the Supporting Information we describe in detail the data, parameters, and curriculum used to train both the DLWP, DLOM, and the diagnostic precipitation module.

## 3 Weather and Climate of DLESyM

Extratropical cyclones (ETC) modulate the day-to-day cool-season weather through the passage of low and high pressure systems. A single severe ETC can cause catastrophic flooding, widespread power outages, and significant fatalities (Busby et al., 2023; Henley & correspondent, 2023). Medium range DL weather forecast models have demonstrated

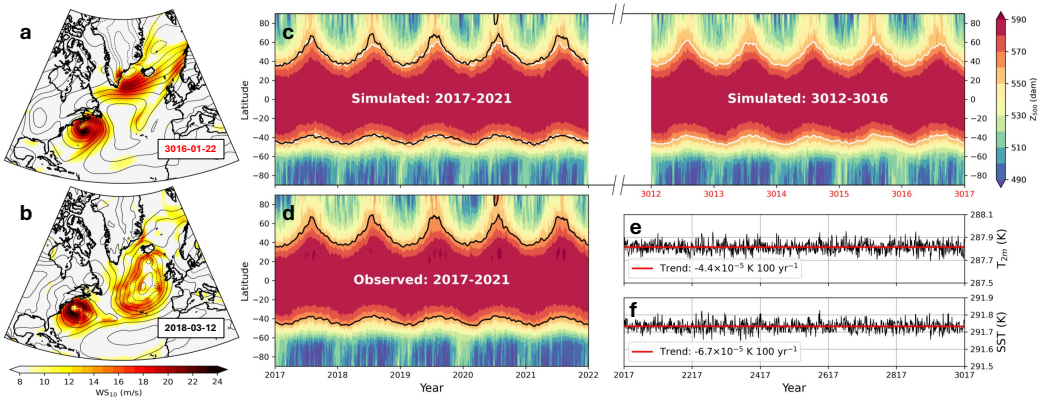


**Figure 2. Multi-century DLESyM simulations continually generate high amplitude features as well as correct representations of current global climate.** Contours of  $Z_{1000}$  (black) and 10-m wind speed (color fill) for (a) a simulated ETC on January 22, 3016 and (b) observed storm on March 3, 2018. Zonally averaged 3-day mean of  $Z_{500}$  plotted as a function of time and latitude: (c) for the first and last 5 years of a recursive 1,000-year model simulation initialized on 1 January 2017 (d) corresponding  $Z_{500}$  field from the ERA5 reanalysis for the years 2017-2022. Also plotted are 15-day averaged values for the 560 dam contour for the DLESyM simulation (white line) in (c) and for ERA5 (black line) as a reference in both (c) and (d). Globally averaged annual mean (e)  $T_{2m}$  and (f) SST (black) during the 1,000 year simulation with the linear fit (red) and the trend noted in each panel.

skill in forecasting even severe ETCs at short lead times (Charlton-Perez et al., 2024), but the features forecasted by many of these models are excessively smoothed over longer lead times (Lam et al., 2023; Lang et al., 2024). In contrast, DLESyM spontaneously generates realistic ETCs with sharply defined features throughout a 1000-year simulation (730,000 auto-regressive steps of the atmospheric module). In late January of simulated year 3016, for example, intense surface winds wrap around a 1000-hPa height ( $Z_{1000}$ ) depression forming a strong “Nor’easter” just southeast of Newfoundland Fig. 2a. The simulated storm demonstrates highly realistic structure when compared to an observed Nor’easter from March 12, 2018 (Fig. 2b).

The model’s accurate reproduction of the annual cycle and negligible drift is illustrated in Fig. 2c,d, which shows the first and last 5 years of a 1000-year simulation initialized on January 1, 2017, along with the ERA5 verification for the period 2017–2021. The field contoured as a function of time and latitude in Fig. 2c,d is zonally averaged 500-hPa geopotential height ( $Z_{500}$ ), which is high in the tropics and lowest over the wintertime pole. There is no predictability for the precise atmospheric state beyond roughly two weeks (Smagorinsky, 1963; Mintz, 1964; Leith, 1965), but the climatological annual cycle of  $Z_{500}$  within the first 5 years of the 1,000-year simulation closely resemble that of the reanalysis. Impressively, this climatological seasonal cycle is maintained through the last five years of the 1000-year simulation. Similar DLESyM results generating the same average climate were obtained for 12 shorter 100-year simulations initialized on the first day of the month throughout a full year.

Drift in global-mean values of the simulated fields is an important concern in climate modeling. Any drift must be sufficiently small that it does not mask actual changes from internal variability or anthropogenic forcing such as greenhouse-gas emissions. Despite the DLESyM’s atmospheric and ocean modules being trained separately, there is

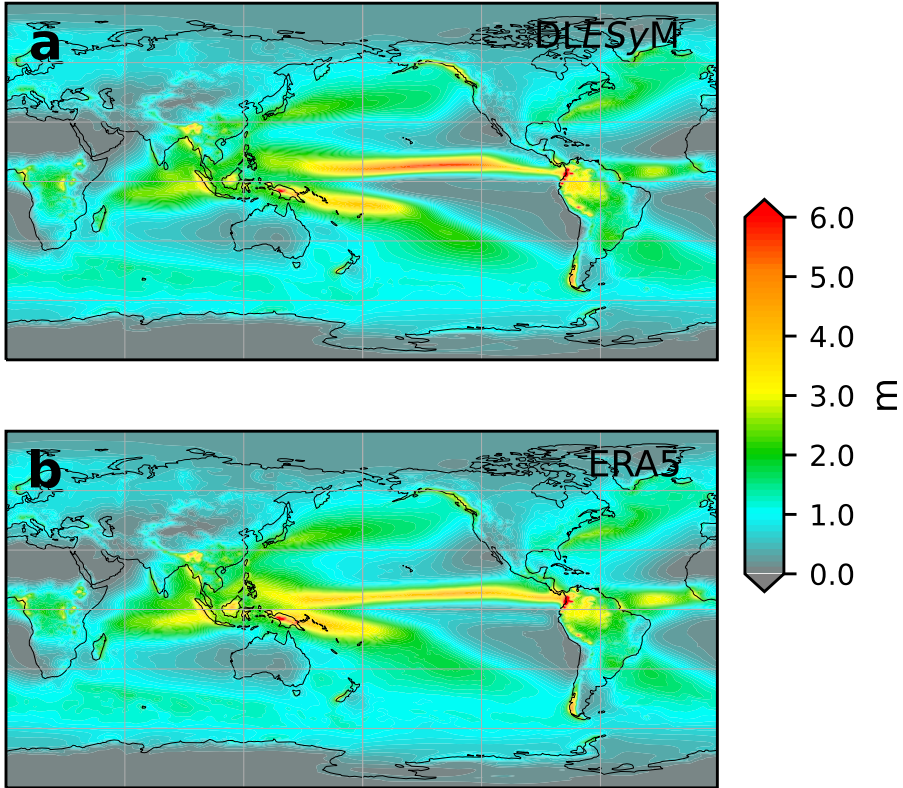


**Figure 3. Climatology of global annual precipitation within DLESyM simulations.** Comparison of annual average precipitation (a) diagnosed from the last 41 years of our 100-year simulation, (b) from ERA5 reanalysis for 1979-2020.

no startup transient or spin-up period in the globally averaged 2-m air temperature and SST, and the long-term drift is negligible (Fig. 2e,f).

Figure 3 shows that the annual averaged precipitation from the last 41 years of our 100-year rollout (Fig. 3a) closely matches ERA5 precipitation for the years 1979-2020 (Fig. 3b), including in regions of heavy precipitation. An exception is in the equatorial Pacific, where the DLESyM over-estimates rainfall in the area of the Intertropical Convergence Zone. Unlike the ISCCP OLR, the ERA5 precipitation is almost exclusively model generated, and therefore subject to error. The actual precipitation is difficult to observe, although analyses such as Integrated Multi-satellitE Retrievals for GPM (IMERG) are available and could be used to train a more realistic precipitation modules. Further discussion of DL precipitation models and their development is left for further study.

#### 4 Tropical Cyclones

Tropical cyclones (TCs) have been responsible for more fatalities than any other single weather event; the 1970 Bhola TC killed 250,000–500,000 people in Bangladesh (Hossain, 2018). The largest TCs in the world are those in the Western North Pacific (WNP) (Chan & Chan, 2015), motivating us to compare the climatology of TC generation over the WNP during the last 30 years of a 100-year simulation from January 1, 2017 with 30 years of ERA5 data and historical simulations from four leading CMIP6 models.

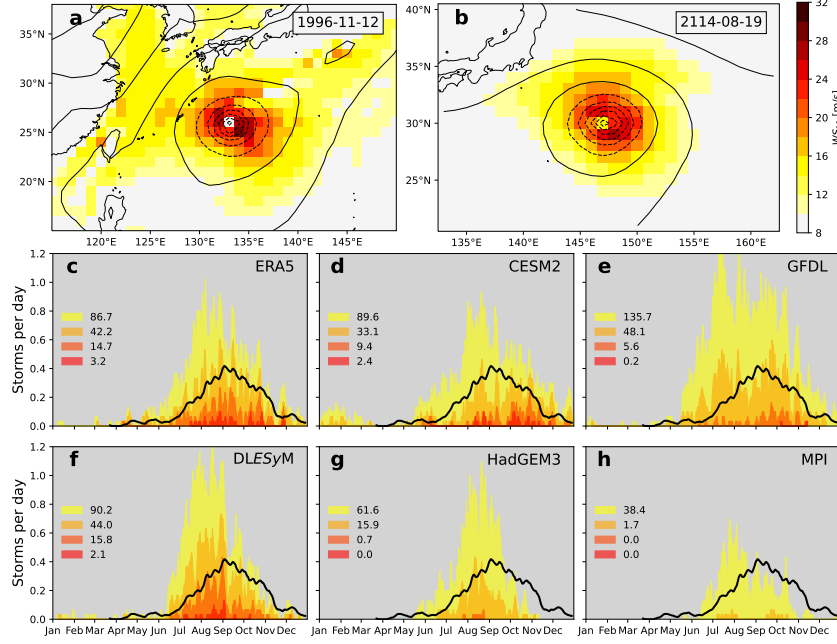


**Figure 4. DLESyM tropical cyclone climatology in WNP compared to those of CMIP6 historical simulations.** (a) ERA5 reanalysis on November 12, 1996 and (b) DLESyM on August 19, 2114 showing  $Z_{1000}$  (black contours, c.i.=6 dkm, contours  $\leq 0$  dkm are dashed) and 10-m wind speeds (color fill). Both ERA5 and DLESyM fields are plotted at  $1^\circ$  latitude-longitude resolution. (c)–(h): average frequency of TCs in storms per day from ERA5 and CMIP6 historical runs from 1985–2014, or 2085–2114 from DLESyM. Average annual number of TCs of Ranks 1–4 is noted in each panel. Black curve in (c)–(h) is the running 20-day average frequency of Rank 2 storms in ERA5.

An example of one of the top ten strongest spontaneously generated TCs near the end of the simulation (in August 2114) is compared with super typhoon Dale from the top ten TCs in the ERA5 reanalysis (on November 12, 1996) in Fig. 4a,b. Both TC have the same amplitude in  $Z_{1000}$ , although the 10-m wind speeds are weaker in the DLESyM simulation, perhaps because of the relatively coarse 110-km grid spacing in our model.

Similarly coarse grid spacing also imposes serious limitations in CMIP6 models. Fig. 4c-h compares the TC frequency in the WNP over the 30-year period 2085–2114 in the DLESyM simulation with the period 1985–2014 in the ERA5 reanalysis and four historical CMIP6 runs. The identification of tropical cyclones is based on the presence of a local minimum in SLP or  $Z_{1000}$ , an upper-level warm core, and at least 2 days of continuity along the same track, as outlined in the Supporting Information. The average number of storms per year, broken down by intensity (see Supporting Information) is also given in each panel. Except for the HadGEM3-GC31-LL, which use a 50% coarser mesh, the CMIP6 results were obtained using roughly the same grid spacing as DLESyM. All four CMIP6 models have difficulty capturing the correct frequency and intensity of TCs in the ERA5 reanalysis, particularly for the stronger storms.

In contrast, the annual average number of TCs spontaneously generated by DLESyM closely matches ERA5. The peak in DLESyM's annual cycle does occur roughly one month early compared to the ERA5 reanalysis, a shift likely produced by a similar one-month shift in the peak SSTs simulated in this region. Recalling the simplicity of our DLOM,

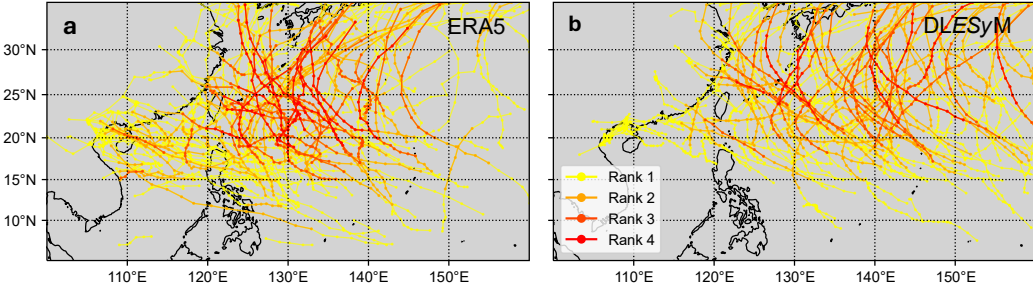


**Figure 5. Tropical cyclone tracks in the Western North Pacific (WNP) are similar in the ERA5 record and DLESyM simulations.** Comparison of TC tracks over a 5-year period from (A) ERA5 (2010-2014), (B) from the DLESyM rollout (2110–2114). These tracks use data at 6-h time resolution, with ranks 1–4 representing storms that, at their highest intensity exceed thresholds corresponding to approximately the 1st, 0.1st, 0.01st, and 0.001st percentile  $Z_{1000}$  values in warm core systems over the western North Pacific region.

this shift might be reduced using a more complete ocean model. Tropical cyclone tracks are similar in ERA5 and the DLESyM simulation (Fig. 5), although the region susceptible to TC activity extend farther to the east in our DLESyM simulation than in observations.

## 5 Atmospheric Blocking in DLESyM

Blocking is produced by high-amplitude ridges that steer atmospheric flows along extended north-south trajectories leading ETCs to detour around the region underneath the ridge (Rex, 1950; Woollings, 2010; Lupo, 2021). Examples of blocking from ERA5 on February 14, 2017 and 1,000 years into the simulation on January 2, 3016 are shown by the northward extension of the  $Z_{500}$  field over western Europe in Fig. 6a,b. Blocking generates anomalous temperature and precipitation patterns that may include extreme cold-air outbreaks (Cattiaux et al., 2010; Whan et al., 2016), heat waves (Barriopedro et al., 2011), droughts and floods (Bissolli et al., 2011; Houze et al., 2011).

Correctly capturing subseasonal and seasonal variability requires Earth System models to faithfully reproduce the frequency, spatial distribution, and amplitude of blocking events. The simulation of blocking events is a challenge for the CMIP6 models (Schiemann et al., 2017; Davini & D’Andrea, 2020) and provides a good test of the climatology in the long-rollout DLESyM simulations. Here we compare the 40-year periods 2070-2110 from a 100-year DLESyM simulation starting on January 1, 2017 with ERA5 reanalysis and CMIP6 historical runs for the period 1970-2010.

The presence of blocking is assessed using the absolute geopotential index introduced by (Tibaldi & Molteni, 1990) with parameters as defined in (Schiemann et al., 2020) and code adapted from the repository published with (Brunner & Steiner, 2017). The time-mean blocking frequency is evaluated pointwise throughout the domain and plotted in units of blocks per day. The CMIP6 models used for these historical runs are the CESM2, GFDL-CM4, HadGEM3-GC31-LL and MPI-ESM1-2-HR.

DLESyM closely approximates the spatial distribution of blocking frequencies computed from ERA5, just slightly underestimating its frequency over Northern Europe, and the Chuckchi sea (Fig 6c,f). The DLESyM result visually appears to match the pattern

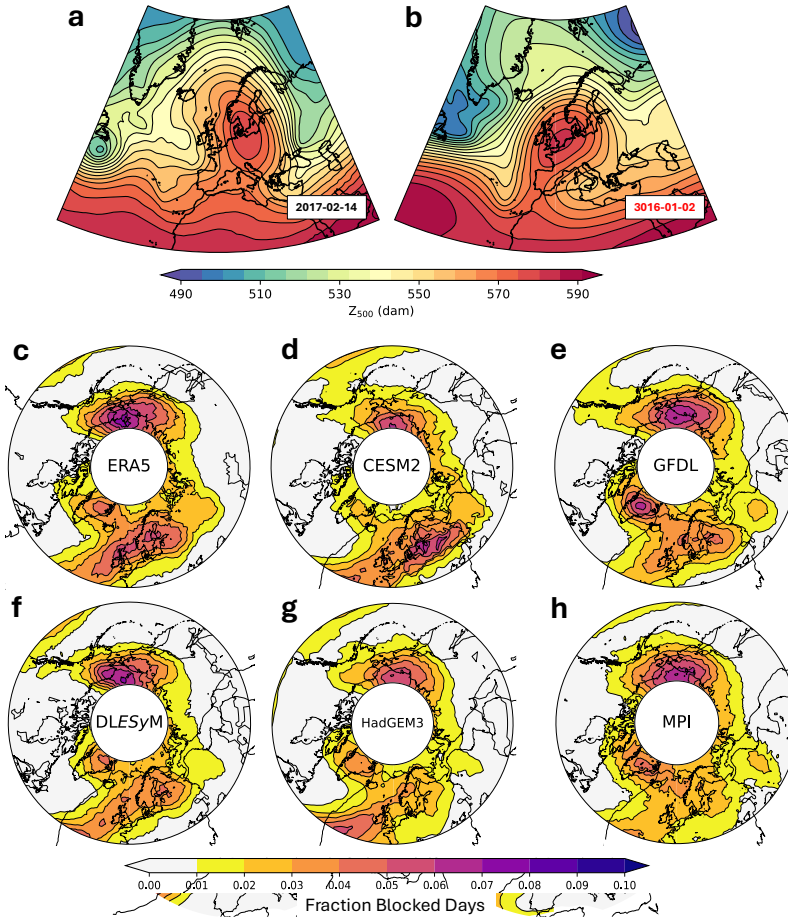


**Figure 6. Representation of atmospheric blocking compared to CMIP6 historical simulations.** Contours of 500-hPa height showing blocking over Western Europe as (a) observed on February 14, 2017, (b) generated near the end of the 1000-y DLESyM simulation on January 2, 2016. Mean frequency of northern hemisphere blocking (c) from ERA5 (1970-2010), (d, e, g, h) as in (c) computed for the same period in historical CMIP6 simulations, and (f) from the last 40 years of the 100-year DLESyM rollout. Source models are identified in the center of each polar projection.

in ERA5 better than the corresponding results from the four CMIP6 models shown in Fig. 6d,e,g,h. The performance of each model against ERA5 is quantified in the Taylor diagram in Fig. 7c.

Taylor diagrams offer a visual assessment of several quantitative aspects of fidelity between simulated and observed fields (Taylor, 2001; Rochford, 2016). Points are plotted on the Taylor diagram in a cylindrical coordinate system. The radial distance at which a point is plotted is the ratio of the standard deviation of the field under evaluation to the standard deviation of the ERA5 target field. The angle at which the point is plotted is given by the inverse cosine of the pattern correlation between the field under evaluation and the ERA5 target. The ERA5 target point is plotted where it would appear if it were the field subjected to evaluation: on the abscissa at a radial distance of unity. The centered pattern RMSE is given by the distance between the point for the field under evaluation and ERA5 target point on the abscissa.

As shown in Fig. 7c, the pattern correlation and centered RMSE for the DLESyM blocking climatology are superior to those for all four CMIP models. DLESyM's ratio of the standard deviation of blocking frequency to that in ERA5 is slightly worse than in the CESM2, but similar or superior to that in the other CMIP6 models.

## 6 Annular Modes

On seasonal and interannual time scales, the most important patterns of extratropical hemispheric-scale variability are the Northern and Southern Annular Modes (the NAM and SAM). High magnitudes of the NAM index are associated with statistically significant changes in the probability of impactful weather, including cold-air outbreaks and intense mid-latitude storms (Thompson & Wallace, 2001).

The Northern Annular Mode (NAM), also commonly referred to as the Arctic Oscillation, is defined as the first Empirical Orthogonal Function (EOF) of the wintertime (November-April) monthly mean  $Z_{1000}$  anomalies north of 20°N (Thompson & Wallace, 1998; Baldwin & Dunkerton, 2001). The anomalies are first calculated by subtracting the climatology (seasonal cycle) at each latitude, longitude, and day of year, and then weighted by the square root of the cosine of latitude before determining the EOF. Daily values of the NAM are obtained by projecting daily anomalies onto the leading EOF patterns.

The positive phase of the spatial pattern of the NAM in ERA5 features a tri-pole pattern: with low heights in the arctic flanked by high heights over the North Pacific and the Atlantic spreading into Western Europe (Fig. 8a). The corresponding anomaly centers are similarly arranged in the DLESyM climatology, although the heights are too strong over the North Pacific. Similar high biases over the North Pacific are also present in the CESM2, MPI, and HadGEM3 climatologies. The percentages in the upper right corner in all panels in Fig. 8 show the percent variance within the full field described by each mode. DLESyM, GFDL, and MPI show contributions from their NAM similar to that of ERA5, while CESM2 and HadGEM3 overestimate the contribution.

The Southern Annular Mode (SAM) is calculated similarly to the NAM but for year-round monthly mean  $Z_{500}$  anomalies south of 20°S.  $Z_{500}$  is used instead of  $Z_{1000}$  to avoid reduction-to-sea-level errors over the high terrain in Antarctica. Maps of this analysis are shown in Fig. 8 g–l. DLESyM expresses a realistic SAM with similar spatial structure and magnitude to the leading mode within ERA5. There is slightly less amplitude in the DLESyM-simulated high centered over the Falkland Islands than the ERA5 record. Similar underestimation is visible in the CMIP6 models as well.

The overall performance of the DLESyM and CMIP6 models are compared against the ERA5 NAM in the Taylor diagram in Fig. 7a. Both the GFDL and MPI models are

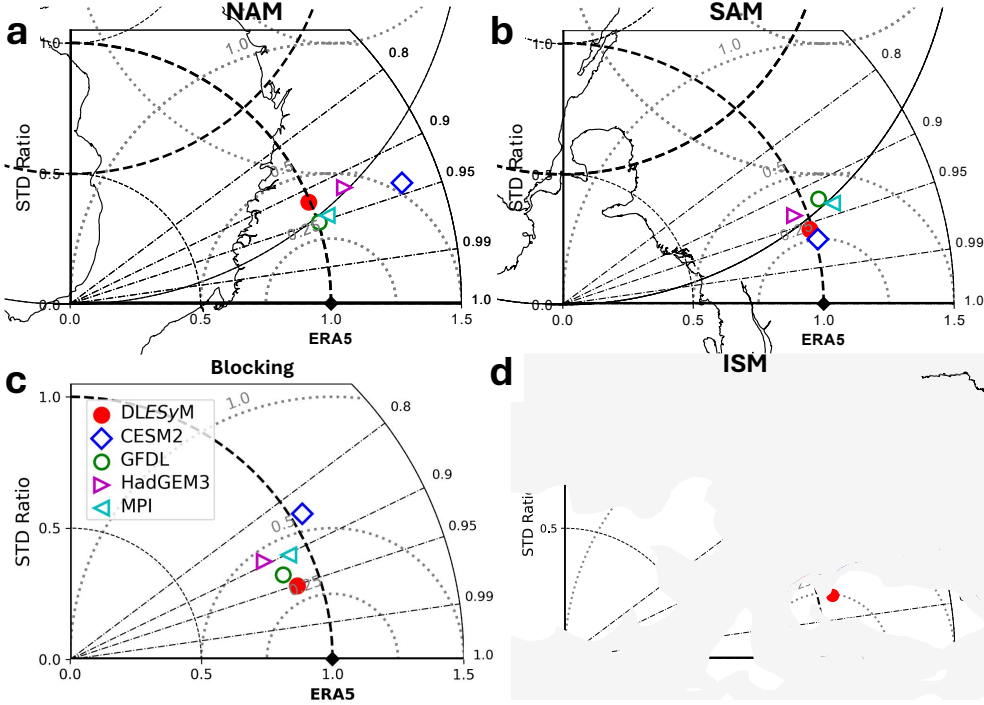


**Figure 7. Quantitative comparison of extra-tropical variability and the seasonal cycle of the Indian Summer monsoon between DLESyM and CMIP6 models.** Taylor diagrams comparing the (a) NAM (Fig. 8a-f) (b) SAM (Fig. 8g-l), and (c) blocking frequency (Fig. 6) in DLESyM for the last 40 years of the 100-year January 1, 2017 simulation and CMIP6 historical simulations for the years 1970-2010 against the same 1970-2010 period in the ERA5 reanalysis. The spatio-temporal OLR signatures plotted in Fig. 9 of the Indian summer monsoon from ISCCP are compared in (d) for years 2085-2114 of the DLESyM simulation with CMIP6 historical runs for 2085-2114. Points are plotted in a cylindrical coordinate system, with radial distance equal to the ratio of the standard deviation of the field under evaluation to the standard deviation of the target field. The angle at which a point is plotted is given by the inverse cosine of the pattern correlation between the field under evaluation and the target. The centered pattern RMSE is given by the distance between a point and the target point on the abscissa. Compared with the collection of four CMIP6 models, the RMSE for DLESyM ranks 3rd out of 5 for the NAM, 2nd out of 5 for the SAM, and first for blocking and the ISM seasonal cycle.

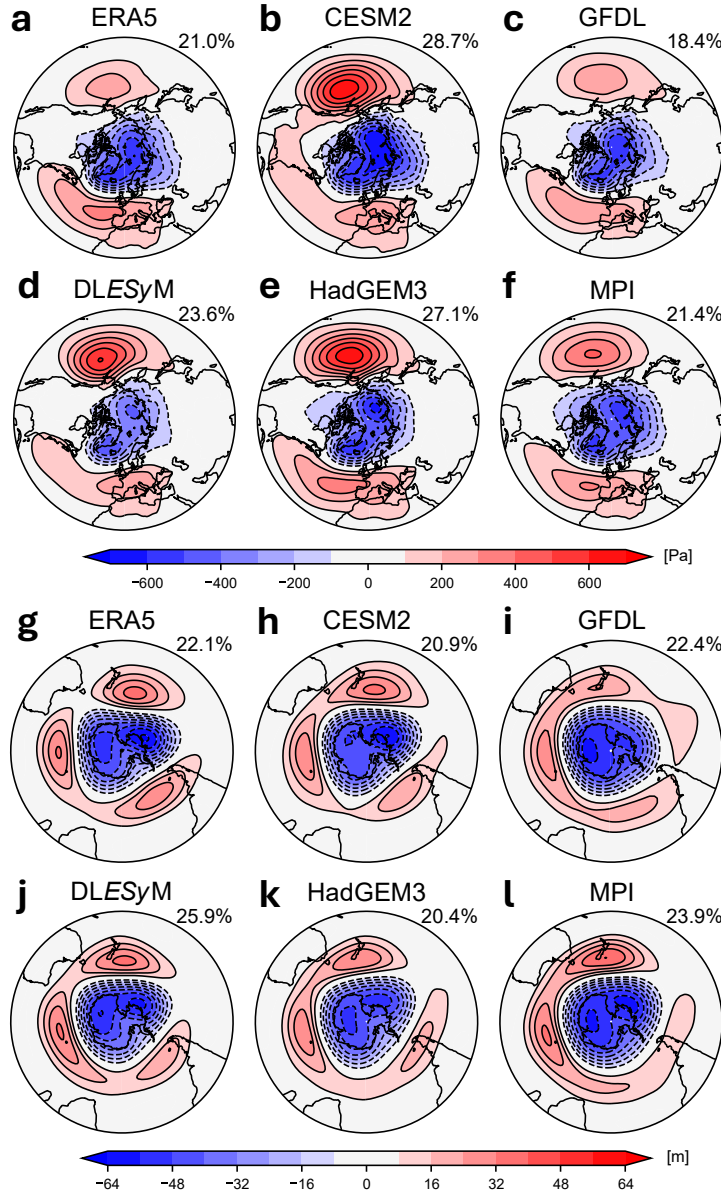


**Figure 8. Comparison of leading modes of extratropical variability between DLESyM and CMIP6 models.** Leading empirical orthogonal function (EOF) of NH variability, the Northern Annular Mode (NAM) in (a) ERA5  $Z_{1000}$  during 1970-2010; (b) SLP simulated by CESM2 for CMIP6 historical experiment; (c,e,f) as in (b) except using GFDL-CM4, HadGEM3-GC31-LL, and MPI-ESM1-2-HR respectively. (d) shows same analysis as (a) evaluated over the last 40 years of the 100 year DLESyM rollout. Leading EOF of SH  $Z_{500}$  variability, the Southern Annular Mode (SAM), in (g) ERA5 during 1970-2010; (h) simulated by CESM2 for CMIP6 historical experiment; (i, k, l) as in (b) except using GFDL-CM4, HadGEM3-GC31-LL, and MPI-ESM1-2-HR respectively. (j) shows same analysis as (g) evaluated over the last 40 years of the 100 year DLESyM rollout. Percentage of explained variance its shown in the upper right of each panel.

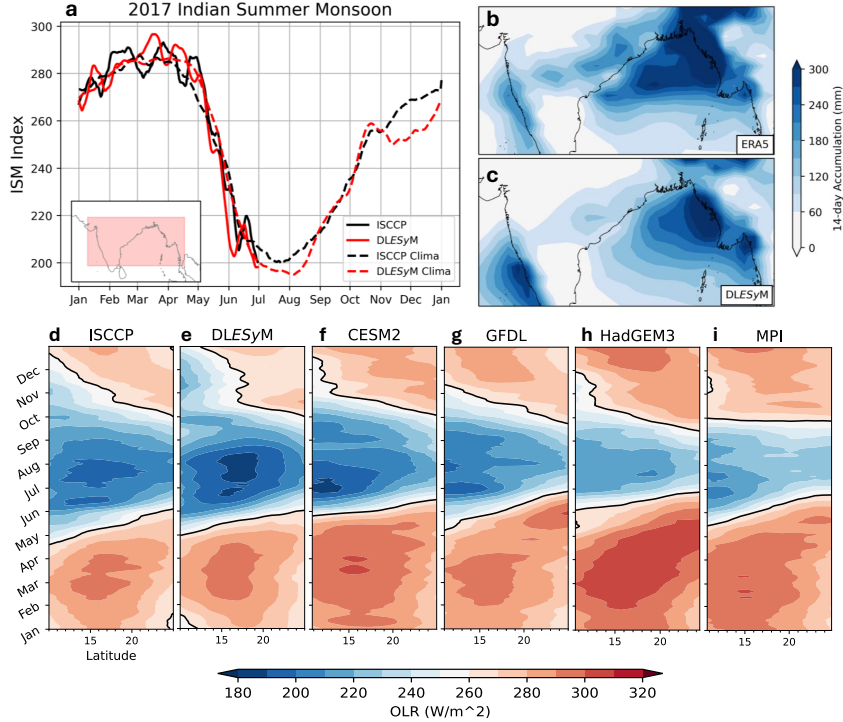


**Figure 9. DLESyM’s simulation of satellite-observed cloud-modulated OLR is superior to CMIP6 models over the Indian Summer Monsoon cycle.** ISM forecast and climatology in DLESyM. (a) Time series of forecasted 2017 ISM index (solid lines) and 30-year climatological index (dashed lines) for DLESyM (red) and ISCCP (black). ISM index is the OLR averaged over the red box on inserted map. 14-day accumulated precipitation beginning June 12, 2017 for (b) ERA5 and (c) DLESyM 6-month forecast initialized January 1, 2017. Annual cycle of north-south progression of OLR averaged zonally across the red box for 1985-2014 from (d) ISCCP observations, (f)-(i) CMIP6 historical simulations and (e) years 2085-2114 of the DLESyM simulation.

superior to DLESyM, which in turn scores better than the other two CMIP6 models. The Taylor diagram for the SAM (Fig. 7b) shows DLESyM clearly outperforms three of the four CMIP6 models, only lagging behind CESM2.

## 7 Indian Summer Monsoon

The Indian summer monsoon (ISM) is a dominant feature in the annual cycle of tropical weather and has a crucial impact on agriculture. Increases or decreases of at least 10% in ISM rainfall have been associated with average deviations of  $\pm 10\%$  in foodgrain production (Parthasarathy et al., 1988). First, we characterize the ISM by its signature in OLR, which in contrast to precipitation, can be easily observed by satellite. The 30-year mean annual cycle of the ISM index (after B. Wang & Fan, 1999; details provided in Supporting Information). Over the period 1985-2014 the ISM in the ISCCP data closely matches that for years 2085-2114 in the 100-year DLESyM simulation through the start of November, after which the DLESyM’s ISM index increases more slowly than in ISCCP (Fig. 9a).

The northward march of zonally averaged ISM convective cloud systems (low OLR) during onset, and their subsequent retreat to the south is plotted for 1985-2014 ISCCP data and 2085-2114 DLESyM simulation in Fig. 9d,e; both show very similar patterns except in November and December, south of  $17^{\circ}$  where DLESyM's OLR values are too low over southern India and the adjacent Indian Ocean. Similarly, the four CMIP6 models have difficulty precisely capturing the annual cycle of the ISM in their simulated OLR fields (Fig. 9f,g,h,i). A quantitative comparison of each model's representation of the ISM is shown as a Taylor diagram (Fig. 7d). DLESyM's ISM climatology of meridionally resolved monsoon onset has superior pattern correlation and centered RMSE to that of the four CMIP6 models when compared to ISCCP observations.

Turning from climatologies to a seasonal forecast, the OLR fields for a six-month DLESyM forecast beginning January 1, 2017 are compared against observations up to the end of the available ISCCP data record. The forecast for the ISM index closely follows ISCCP observations, although much of this skill is derived from accurate representation of the strong climatological seasonality (Fig. 9a). Two-week averaged regional precipitation predicted at the end of the 6-month DLESyM forecast is similar to the ERA5 verification (Fig. 9b,c). Further comparison of the DLESyM forecast and ERA5 precipitation during the 2017 monsoon onset is included in Supporting Information.

## 8 El Niño

The El Niño Southern Oscillation (ENSO) is the leading mode of interannual variability and impacts global weather patterns including precipitation over North America (Ropelewski & Halpert, 1986), the duration of the South Asian Monsoon (Goswami & Xavier, 2005), and the frequency of Atlantic hurricanes (Gray, 1984). DLESyM spontaneously generates temporal variations in the Niño 3.4 region ( $5^{\circ}\text{N}$ – $5^{\circ}\text{S}$ ,  $170^{\circ}\text{W}$ – $120^{\circ}\text{W}$ ) comparable to observations, albeit weaker in magnitude (Fig. 10a). There is no tendency for the model to drift toward a warm or cold state in the equatorial Pacific. Instead, weak El Niños or La Niñas with magnitudes of the Niño 3.4 index exceeding 0.5 develop with a period of roughly 4 years, consistent with observations.

To assess patterns of spatial variability, SST and OLR anomalies for observations (Fig. 10b,c) and model output (Fig. 10d,e) are regressed onto their respective standardized Niño 3.4 times series. Maps of these regression coefficients, interpreted as the SST and OLR anomalies associated with a positive one standard-deviation of the Niño 3.4 index, reveal that DLESyM generates patterns of variability remarkably consistent with observations. Associated with positive Niño 3.4 anomalies, DLESyM exhibits widespread warming and cooling in the eastern and western Pacific, respectively, and a weakening of the climatological west-east equatorial SST gradient. Coincident with this pattern of SST changes is a decrease in OLR in the central Pacific consistent with high cloud-tops, deep convection, and a shift in the Walker circulation. Positive Niño 3.4 anomalies are also associated with an increase in OLR in the western Pacific, characteristic of subsidence and reduced cloud cover. Moreover, the similarity between the DLESyM and observed response pattern of SSTs and OLR in remote ocean basins (i.e. Atlantic and Southern Oceans) suggests DLESyM may capture the remote atmospheric teleconnections associated with ENSO.

Despite the low amplitude in DLESyM's ENSO, these results strongly suggest that, with modest improvements, DLESyM can be a powerful new tool for studying ENSO variability. Recall that the ocean module in DLESyM is quite basic, predicting only SSTs. A more complete model capable of capturing atmosphere-ocean interactions, thermal damping, and upper-ocean dynamics is being developed to better capture realistic ENSO amplitudes.

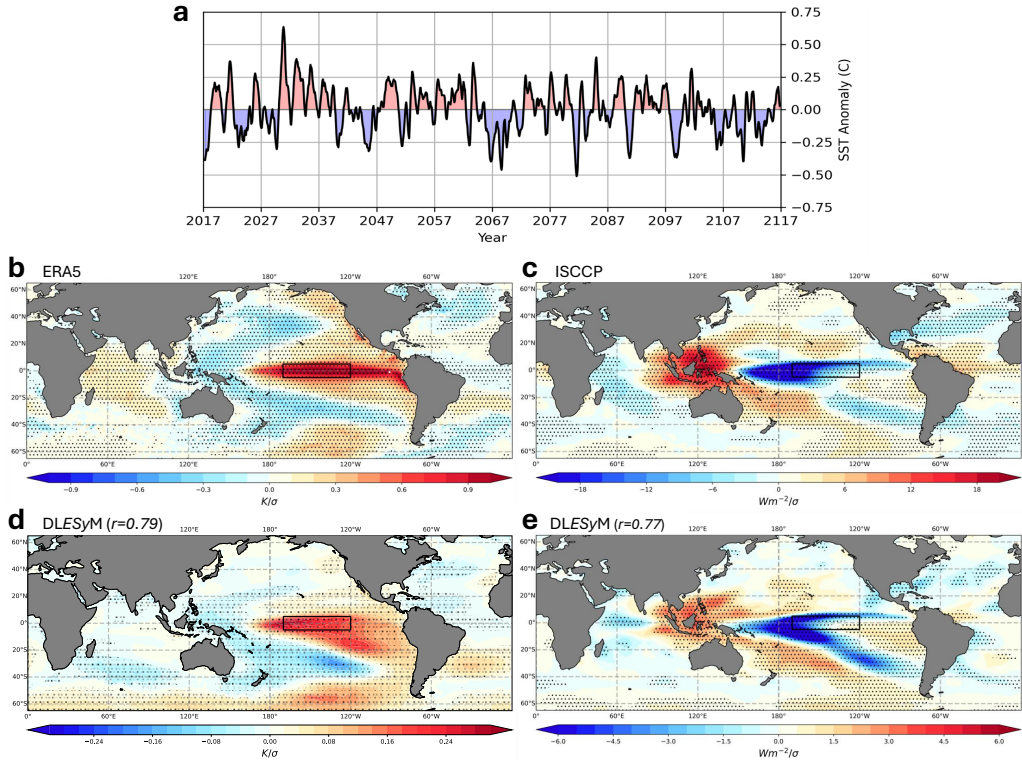


**Figure 10. El Niño Southern Oscillation variability and teleconnections in DLESyM.** (a) Niño 3.4 index (5N-5S, 170W-120W; black box) computed from the perturbation of the equatorial SSTs from the monthly climatology in the 100-year rollout. Anomalies of (b) ERA5 SST, (c) ISCCP OLR, (d) DLESyM SST, and (e) DLESyM OLR regressed onto their respective standardized Niño 3.4 time series. Stippling indicates statistical significance ( $p \leq 0.05$ ) in similarity to the verification, computed from a 2-tailed p-value associated with Pearson correlation coefficient. Correlations between modeled and observed regression maps are given in parenthetical  $r$  values beside subplot titles d and e.

## 9 Conclusion

Efforts to improve SOTA Earth System models often focus on incorporating increasingly detailed representations of additional physical processes and extending to higher spatial resolutions. As a result, using these traditional models becomes increasingly difficult for those without access to very high performance computing. Here we adopt a simpler and novel approach, asynchronously coupling a DLWP model with just 9 prognostic variables to a DLOM simulating SST, both using a 110-km globally-uniform mesh. The resulting *DLESyM* reproduces several aspects of the current climate at least as well as leading CMIP6 models at similar spatial resolution, yet as configured for this investigation, the *DLESyM* can complete a 1000-year simulation on a single NVIDIA A100 GPU in about 12 h. In contrast, running a 1000-year simulation with the National Center for Atmospheric Research’s CESM2.1.5 model at similar spatial resolution using 1280 processing elements on their HPE Cray EX, would take approximately 90 days.

The simulations shown here demonstrate that our *DLESyM* is not subject to several limitations that have been assumed to apply to the stability and accuracy of long autoregressive rollouts of deep learning Earth System and weather forecast models (Lam et al., 2023; Price et al., 2024; Chattopadhyay & Hassanzadeh, 2023). In particular, the *DLESyM* simulation remains stable for 730,000 atmospheric-module steps without significantly smoothing the structure of individual weather systems. Empiricism clearly underlies our data-driven machine learning approach, while playing a lesser role in traditional Earth System models. CMIP models do, nevertheless, also include many empirically tuned parameters. For example, parameters are typically adjusted to minimize any drift in pre-industrial climate simulations remaining after an initial spin up period of several centuries. In contrast, there is no initial transience when our separately trained atmosphere and ocean models begin the coupled simulation, and drifts in *DLESyM*’s globally averaged 2-m air temperature and SST are negligible.

Surprisingly, the robust long-term properties of the *DLESyM* emerge after training it on loss functions that only focus on very short-term performance. Those loss functions consist of RMSE averaged over one day in the atmosphere and eight days in the ocean. No physical constraints or components of the training loss explicitly push the model toward the correct long-term behavior.

Climatologies of 30- and 40-year periods from long iterative *DLESyM* simulations were compared to similar length periods from the ERA5 reanalysis, ISCCP satellite observations, and historical runs from four CMIP models. The frequency and spatial distribution of northern-hemisphere blocking is captured by *DLESyM* at least as well as by the CMIP6 models. In the tropics, *DLESyM* rollouts replicate the observed daily climatology of tropical cyclones in the western North Pacific and the Indian Summer monsoon better than the CMIP6 models. The northern and southern annular modes (NAM and SAM) are captured with fidelity similar to the CMIP6 models as measured by spatial correlation, variance, and RMSE. Because both the NAM and SAM are associated with extreme weather, long simulations of *DLESyM* can help us understand the statistics of extreme weather patterns.

One limitation of *DLESyM* is that it is only suitable for simulations of the current climate. It remains, however, a powerful tool to study internal climate variability, and offers a radical increase in the accessibility of a high fidelity Earth System model. By accurately capturing variability across timescales, *DLESyM* shows great promise for use in seasonal and subseasonal forecasting (S2S). Improved S2S forecasts, in particular, have the potential for immediate societal benefit. Indeed, ensemble *DLESyM* forecasts are currently being developed for this purpose but are left as the topic of future work. Forecasts of future climates will require the model to incorporate forcing from greenhouse gases and anthropogenic aerosols; further investigation is warranted to determine whether this can be achieved by adding physical constraints to the model.

## Open Research Section

All data used in this study was obtained through publicly available data repositories. ERA5 data was downloaded from ECMWF’s Climate Data Store (Hersbach et al., 2020; Copernicus Climate Change Service, 2018). ISCCP data is made available by NOAA’s National Center for Environmental Information initiative (Young et al., 2018; *International Satellite Cloud Climatology Project (ISCCP)-H Series*, 2021). Code required for data preparation, model training/inference, and analysis is published on GitHub (<https://github.com/AtmosSciDLESyM/DLESyM>). CMIP6 data was downloaded using the accmip6 open source project (Mozumder, 2019).

## Author Contributions

DLESyM conceptualization: DRD, NCC. Model development: NCC, MK, ZL. DLESyM training: NCC. Precipitation module conceptualization: DRD and RM. Precipitation module training: RM. DLESyM Execution of rollouts: NCC. Data curation: NCC, ZL, MK, BL, RM. Analysis design: DRD, NCC, BL, ZE. Analysis execution: BL, NCC, ZE, RM. Writing: DRD, NCC, BL, ZE, RM. Revisions: NCC, DRD, ZE, MK, BL, RM, ZL. Figures: BL, NCC, RM, ZE, DRD. Project coordination: DRD.

## Acknowledgments

We thank Mike Pritchard and David Battisti for thoughtful comments on the manuscript. We thank Zilu Meng for comments on calculation of blocking frequency. We thank the Earth System Grid Federation (ESGF) for facilitating access to CMIP6 data. This research was supported by the Office of Naval Research under grants N0014-21-1-2827, N00014-22-1-2807, and N00014-24-12528. This work was supported in part by high-performance computer time and resources from the DoD High Performance Computing Modernization Program. NCC was supported by a National Defense Science and Engineering Graduate Fellowship. BL was supported by the Joint Ph.D. Training Program of the University of Chinese Academy of Sciences, and by the National Science Foundation of China (42075052). MK was supported by the Deutscher Akademischer Austauschdienst (DAAD, German Academic Exchange Service), by the International Max Planck Research School for Intelligent Systems (IMPRS-IS), and by the Deutsche Forschungsgemeinschaft (DFG, German Research Foundation) under Germany’s Excellence Strategy EXC 2064 – 390727645. ZE was supported by the U.S. Department of Energy, Office of Science, Office of Advanced Scientific Computing Research, Department of Energy Computational Science Graduate Fellowship under Award Number DE-SC0023112. We are grateful to NVIDIA and Stan Posey for the donation of A100 GPU cards. This research was additionally supported by a grant from the NVIDIA Applied Research Accelerator Program and utilized a NVIDIA DGX-100 Workstation. Finally, this work benefited substantially from the barrier-free high quality ERA5 dataset provided by the ECMWF.

This report was prepared as an account of work sponsored by an agency of the United States Government. Neither the United States Government nor any agency thereof, nor any of their employees, makes any warranty, express or implied, or assumes any legal liability or responsibility for the accuracy, completeness, or usefulness of any information, apparatus, product, or process disclosed, or represents that its use would not infringe privately owned rights. Reference herein to any specific commercial product, process, or service by trade name, trademark, manufacturer, or otherwise does not necessarily constitute or imply its endorsement, recommendation, or favoring by the United States Government or any agency thereof. The views and opinions of authors expressed herein do not necessarily state or reflect those of the United States Government or any agency thereof.

## Conflict of Interest Statement

The authors have no conflicts of interest to declare.

## References

Arcomano, T., Szunyogh, I., Wikner, A., Hunt, B. R., & Ott, E. (2023). A hybrid atmospheric model incorporating machine learning can capture dynamical processes not captured by its physics-based component. *Geophysical Research Letters*, 50(8), e2022GL102649. doi: 10.1029/2022GL102649

Baldwin, M. P., & Dunkerton, T. J. (2001). Stratospheric Harbingers of Anomalous Weather Regimes. *Science*, 294(5542), 581–584. Retrieved 2024-07-26, from <https://www.science.org/doi/10.1126/science.1063315> doi: 10.1126/science.1063315

Ballas, N., Yao, L., Pal, C., & Courville, A. (2015). Delving deeper into convolutional networks for learning video representations. *arXiv preprint arXiv:1511.06432*.

Barriopedro, D., Fischer, E. M., Luterbacher, J., Trigo, R. M., & García-Herrera, R. (2011). The Hot Summer of 2010: Redrawing the Temperature Record Map of Europe. *Science*, 332(6026), 220–224. Retrieved 2024-05-21, from <https://www.jstor.org/stable/29784030>

Bi, K., Xie, L., Zhang, H., Chen, X., Gu, X., & Tian, Q. (2023). Accurate medium-range global weather forecasting with 3D neural networks. *Nature*, 619(7970), 533–538. Retrieved 2024-02-12, from <https://www.nature.com/articles/s41586-023-06185-3> doi: 10.1038/s41586-023-06185-3

Bissolli, P., Friedrich, K., Rapp, J., & Ziese, M. (2011). Flooding in eastern central Europe in May 2010 – reasons, evolution and climatological assessment. *Weather*, 66(6), 147–153. doi: 10.1002/wea.759

Brunner, L., & Steiner, A. K. (2017). A global perspective on atmospheric blocking using GPS radio occultation – one decade of observations. *Atmospheric Measurement Techniques*, 10(12), 4727–4745. Retrieved 2024-08-01, from <https://amt.copernicus.org/articles/10/4727/2017/> doi: 10.5194/amt-10-4727-2017

Busby, M., Bryant, M., Bayer, L., Bryant, M. B. n. M., & Bayer (earlier), L. (2023). Storm Ciarán: deaths reported across Europe while UK faces major disruption – as it happened. *the Guardian*. Retrieved 2024-07-23, from <https://www.theguardian.com/world/live/2023/nov/02/storm-ciaran-live-latest-updates-uk-weather-europe>

Cattiaux, J., Vautard, R., Cassou, C., Yiou, P., Masson-Delmotte, V., & Codron, F. (2010). Winter 2010 in Europe: A cold extreme in a warming climate. *Geophysical Research Letters*, 37(20). Retrieved 2024-05-21, from <https://onlinelibrary.wiley.com/doi/abs/10.1029/2010GL044613> doi: 10.1029/2010GL044613

Chan, K. T. F., & Chan, J. C. L. (2015). Global climatology of tropical cyclone size as inferred from QUIKSCAT data. *International Journal of Climatology*, 35(15), 4843–4848. doi: 10.1002/joc.4307

Charlton-Perez, A. J., Dacre, H. F., Driscoll, S., Gray, S. L., Harvey, B., Harvey, N. J., ... Volonté, A. (2024). Do AI models produce better weather forecasts than physics-based models? A quantitative evaluation case study of Storm Ciarán. *npj Climate and Atmospheric Science*, 7(1), 1–11. doi: 10.1038/s41612-024-00638-w

Chattpadhyay, A., & Hassanzadeh, P. (2023). Long-term instabilities of deep learning-based digital twins of the climate system: The cause and a solution. *arXiv:2304.07029*. doi: 10.48550/arXiv.2304.07029

Chen, K., Han, T., Gong, J., Bai, L., Ling, F., Luo, J.-J., ... Ouyang, W. (2023).

FengWu: Pushing the Skillful Global Medium-range Weather Forecast beyond 10 Days Lead. *arXiv:2304.02948*. doi: 10.48550/arXiv.2304.02948

Chen, L., Zhong, X., Zhang, F., Cheng, Y., Xu, Y., Qi, Y., & Li, H. (2023). FuXi: A cascade machine learning forecasting system for 15-day global weather forecast. *npj Climate and Atmospheric Science*, 6(1), 1–11. doi: 10.1038/s41612-023-00512-1

Clark, S. K., Watt-Meyer, O., Kwa, A., McGibbon, J., Henn, B., Perkins, W. A., ... Bretherton, C. S. (2024). *ACE2-SOM: Coupling an ML atmospheric emulator to a slab ocean and learning the sensitivity of climate to changed CO<sub>2</sub>* (No. arXiv:2412.04418). arXiv. Retrieved 2025-01-09, from <http://arxiv.org/abs/2412.04418> doi: 10.48550/arXiv.2412.04418

Copernicus Climate Change Service. (2018). *ERA5 hourly data on pressure levels from 1940 to present*. Copernicus Climate Change Service (C3S) Climate Data Store (CDS). Retrieved 2024-09-17, from <https://cds.climate.copernicus.eu/doi/10.24381/cds.bd0915c6> doi: 10.24381/CDS.BD0915C6[Dataset]

Davini, P., & D'Andrea, F. (2020, December). From CMIP3 to CMIP6: Northern Hemisphere Atmospheric Blocking Simulation in Present and Future Climate. *Journal of Climate*, 33(23), 10021–10038. doi: 10.1175/JCLI-D-19-0862.1

de Burgh-Day, C. O., & Leeuwenburg, T. (2023, November). Machine learning for numerical weather and climate modelling: A review. *Geoscientific Model Development*, 16(22), 6433–6477. doi: 10.5194/gmd-16-6433-2023

Eyring, V., Bony, S., Meehl, G. A., Senior, C. A., Stevens, B., Stouffer, R. J., & Taylor, K. E. (2016). Overview of the Coupled Model Intercomparison Project Phase 6 (CMIP6) experimental design and organization. *Geoscientific Model Development*, 9(5), 1937–1958. doi: 10.5194/gmd-9-1937-2016

Goswami, B. N., & Xavier, P. K. (2005). Enso control on the south asian monsoon through the length of the rainy season. *Geophysical Research Letters*, 32(18).

Gray, W. M. (1984, September). Atlantic Seasonal Hurricane Frequency. Part I: El Niño and 30 mb Quasi-Biennial Oscillation Influences. *Monthly Weather Review*, 112(9), 1649–1668. doi: 10.1175/1520-0493(1984)112<1649:ASHFPI>2.0.CO;2

Gupta, A. S., & England, M. H. (2007). Coupled ocean–atmosphere feedback in the southern annular mode. *Journal of Climate*. Retrieved 2025-02-05, from <https://journals.ametsoc.org/view/journals/clim/20/14/jcli4200.1.xml> (Section: Journal of Climate) doi: 10.1175/JCLI4200.1

Górski, K. M., Hivon, E., Banday, A. J., Wandelt, B. D., Hansen, F. K., Reinecke, M., & Bartelmann, M. (2005). HEALPix: A Framework for High-Resolution Discretization and Fast Analysis of Data Distributed on the Sphere. *The Astrophysical Journal*, 622(2), 759. Retrieved 2024-08-05, from <https://dx.doi.org/10.1086/427976> doi: 10.1086/427976

Henley, J., & correspondent, J. H. E. (2023). Storm Ciarán: Seven people killed and dozens injured in Europe. *The Guardian*. Retrieved 2024-07-23, from <https://www.theguardian.com/world/2023/nov/02/storm-ciaran-people-killed-injured-storm-ciaran-batters-europe-wind-rain>

Herceg-Bulić, I., & Kucharski, F. (2014). North atlantic SSTs as a link between the wintertime NAO and the following spring climate. *Journal of Climate*. Retrieved 2025-02-05, from <https://journals.ametsoc.org/view/journals/clim/27/1/jcli-d-12-00273.1.xml> (Section: Journal of Climate) doi: 10.1175/JCLI-D-12-00273.1

Hersbach, H., Bell, B., Berrisford, P., Hirahara, S., Horányi, A., Muñoz-Sabater, J., ... Thépaut, J.-N. (2020). The ERA5 global reanalysis. *Quarterly Journal of the Royal Meteorological Society*, 146(730), 1999–2049. Retrieved 2024-09-17, from <https://onlinelibrary.wiley.com/doi/abs/10.1002/qj.3803> doi: 10.1002/qj.3803[Dataset]

Hossain, N. (2018). The 1970 Bhola cyclone, nationalist politics, and the subsistence

crisis contract in Bangladesh. *Disasters*, 42(1), 187–203. doi: 10.1111/disa.12235

Houze, R. A., Rasmussen, K. L., Medina, S., Brodzik, S. R., & Romatschke, U. (2011). Anomalous Atmospheric Events Leading to the Summer 2010 Floods in Pakistan. *Bulletin of the American Meteorological Society*, 92(3), 291–298. doi: 10.1175/2010BAMS3173.1

*International satellite cloud climatology project (ISCCP)-h series*. (2021). Retrieved 2025-02-22, from <https://www.nci.noaa.gov/products/international-satellite-cloud-climatology> [Dataset]

Karlbauer, M., Cresswell-Clay, N., Durran, D. R., Moreno, R. A., Kurth, T., Bonev, B., ... Butz, M. V. (2024). Advancing Parsimonious Deep Learning Weather Prediction Using the HEALPix Mesh. *Journal of Advances in Modeling Earth Systems*, 16(8), e2023MS004021. Retrieved 2024-08-29, from <https://onlinelibrary.wiley.com/doi/abs/10.1029/2023MS004021> doi: 10.1029/2023MS004021

Kochkov, D., Yuval, J., Langmore, I., Norgaard, P., Smith, J., Mooers, G., ... Hoyer, S. (2023). *Neural General Circulation Models*. arXiv. Retrieved 2024-02-12, from <http://arxiv.org/abs/2311.07222> (arXiv:2311.07222 [physics])

Lam, R., Sanchez-Gonzalez, A., Willson, M., Wirnsberger, P., Fortunato, M., Alet, F., ... Battaglia, P. (2023). Learning skillful medium-range global weather forecasting. *Science*, 382(6677), 1416–1421. Retrieved 2024-02-12, from <https://www.science.org/doi/10.1126/science.adi2336> doi: 10.1126/science.adi2336

Lang, S., Alexe, M., Chantry, M., Dramsch, J., Pinault, F., Raoult, B., ... Rabier, F. (2024). AIFS - ECMWF's data-driven forecasting system. *arXiv:2406.01465*.

Leith, C. (1965). Methods in computational physics. *New York: Academic*.

Liu, Z., Mao, H., Wu, C.-Y., Feichtinger, C., Darrell, T., & Xie, S. (2022). *A ConvNet for the 2020s*. arXiv. Retrieved 2024-05-26, from <http://arxiv.org/abs/2201.03545> (arXiv:2201.03545) doi: 10.48550/arXiv.2201.03545

Lupo, A. R. (2021). Atmospheric blocking events: a review. *Annals of the New York Academy of Sciences*, 1504, 5–24. doi: 10.1111/nyas.14557

Mann, M. E., Steinman, B. A., & Miller, S. K. (2014). On forced temperature changes, internal variability, and the AMO. *Geophysical Research Letters*, 41(9), 3211–3219. Retrieved 2025-02-05, from <https://onlinelibrary.wiley.com/doi/abs/10.1002/2014GL059233> (eprint: <https://onlinelibrary.wiley.com/doi/pdf/10.1002/2014GL059233>) doi: 10.1002/2014GL059233

Marotzke, J., & Forster, P. M. (2015). Forcing, feedback and internal variability in global temperature trends. *Nature*, 517(7536), 565–570. Retrieved 2025-02-05, from <https://www.nature.com/articles/nature14117> (Publisher: Nature Publishing Group) doi: 10.1038/nature14117

Mintz, Y. (1964). *Very long-term global integration of the primitive equations of atmospheric motion* (No. 111). Secretariat of the World Meteorological Organization.

Mozumder, T. H. (2019). *accmip6: Real-time search and download from continuously updating cmip6 database*. Retrieved from <https://accmip6.readthedocs.io/en/latest/index.html> [Software]

Parthasarathy, B., Munot, A. A., & Kothawale, D. R. (1988, March). Regression model for estimation of Indian foodgrain production from summer monsoon rainfall. *Agricultural and Forest Meteorology*, 42(2), 167–182. doi: 10.1016/0168-1923(88)90075-5

Paszke, A., Gross, S., Massa, F., Lerer, A., Bradbury, J., Chanan, G., ... Chintala, S. (2019). Pytorch: An imperative style, high-performance deep

learning library. In H. Wallach, H. Larochelle, A. Beygelzimer, F. d'Alché-Buc, E. Fox, & R. Garnett (Eds.), *Advances in neural information processing systems 32* (pp. 8024–8035). Curran Associates, Inc. Retrieved from <http://papers.neurips.cc/paper/9015-pytorch-an-imperative-style-high-performance-deep-learning-library.pdf>

Price, I., Sanchez-Gonzalez, A., Alet, F., Ewalds, T., El-Kadi, A., Stott, J., ... Willson, M. (2024). GenCast: Diffusion-based ensemble forecasting for medium-range weather. *arXiv:2312.15796v2*. doi: 10.48550/arXiv.2312.15796v2

Rasp, S., & Thuerey, N. (2021). Data-driven medium-range weather prediction with a resnet pretrained on climate simulations: A new model for weather-bench. *Journal of Advances in Modeling Earth Systems*, 13(2). Retrieved from <https://doi.org/10.1029/2020MS002405> doi: 10.1029/2020MS002405

Rex, D. F. (1950). Blocking Action in the Middle Troposphere and its Effect upon Regional Climate. *Tellus*, 2(4), 275–301. Retrieved 2024-05-21, from <https://onlinelibrary.wiley.com/doi/abs/10.1111/j.2153-3490.1950.tb00339.x> doi: 10.1111/j.2153-3490.1950.tb00339.x

Rochford, P. A. (2016). *Skillmetrics: A python package for calculating the skill of model predictions against observations*. Retrieved from [http://github.com/PeterRochford/SkillMetrics\[Software\]](http://github.com/PeterRochford/SkillMetrics[Software])

Ronneberger, O., Fischer, P., & Brox, T. (2015). U-net: Convolutional networks for biomedical image segmentation. In *Medical image computing and computer-assisted intervention–miccai 2015: 18th international conference, munich, germany, october 5-9, 2015, proceedings, part iii 18* (pp. 234–241).

Ropelewski, C. F., & Halpert, M. S. (1986). North american precipitation and temperature patterns associated with the el niño/southern oscillation (enso). *Monthly Weather Review*, 114(12), 2352–2362.

Schiemann, R., Athanasiadis, P., Barriopedro, D., Doblas-Reyes, F., Lohmann, K., Roberts, M. J., ... Vidale, P. L. (2020). Northern Hemisphere blocking simulation in current climate models: evaluating progress from the Climate Model Intercomparison Project Phase 5 to 6 and sensitivity to resolution. *Weather and Climate Dynamics*, 1(1), 277–292. Retrieved 2024-05-17, from <https://wcd.copernicus.org/articles/1/277/2020/> doi: 10.5194/wcd-1-277-2020

Schiemann, R., Demory, M.-E., Shaffrey, L. C., Strachan, J., Vidale, P. L., Mizieliński, M. S., ... Jung, T. (2017). The Resolution Sensitivity of Northern Hemisphere Blocking in Four 25-km Atmospheric Global Circulation Models. *Journal of Climate*, 30(1), 337–358. Retrieved 2024-05-21, from <https://journals.ametsoc.org/view/journals/clim/30/1/jcli-d-16-0100.1.xml> doi: 10.1175/JCLI-D-16-0100.1

Smagorinsky, J. (1963). General circulation experiments with the primitive equations: I. the basic experiment. *Monthly weather review*, 91(3), 99–164.

Taylor, K. E. (2001, April). Summarizing multiple aspects of model performance in a single diagram. *Journal of Geophysical Research: Atmospheres*, 106(D7), 7183–7192. doi: 10.1029/2000JD900719

Thompson, D. W. J., & Wallace, J. M. (1998). The Arctic oscillation signature in the wintertime geopotential height and temperature fields. *Geophysical Research Letters*, 25(9), 1297–1300. Retrieved 2024-07-26, from <https://onlinelibrary.wiley.com/doi/abs/10.1029/98GL00950> doi: 10.1029/98GL00950

Thompson, D. W. J., & Wallace, J. M. (2001). Regional Climate Impacts of the Northern Hemisphere Annular Mode. *Science*, 293(5527), 85–89. Retrieved 2024-07-26, from <https://www.science.org/doi/10.1126/science.1058958> doi: 10.1126/science.1058958

Tibaldi, S., & Molteni, F. (1990). On the operational predictability of blocking. *Tellus A*, 42(3), 343–365. doi: 10.1034/j.1600-0870.1990.t01-2-00003.x

Ullrich, P. A., Zarzycki, C. M., McClenney, E. E., Pinheiro, M. C., Stansfield, A. M., & Reed, K. A. (2021). Tempestextremes v2. 1: A community framework for feature detection, tracking, and analysis in large datasets. *Geoscientific Model Development*, 14(8), 5023–5048. doi: <https://doi.org/10.5194/gmd-14-5023-2021>

Wang, B., & Fan, Z. (1999, April). Choice of South Asian Summer Monsoon Indices. *Bulletin of the American Meteorological Society*, 80(4), 629–638. doi: 10.1175/1520-0477(1999)080<0629:COSASM>2.0.CO;2

Wang, C., Pritchard, M. S., Brenowitz, N., Cohen, Y., Bonev, B., Kurth, T., ... Pathak, J. (2024). Coupled ocean-atmosphere dynamics in a machine learning earth system model. *arXiv:2406.08632*. doi: 10.48550/arXiv.2406.08632

Watt-Meyer, O., Dredner, G., McGibbon, J., Clark, S. K., Henn, B., Duncan, J., ... Bretherton, C. S. (2023). *ACE: A fast, skillful learned global atmospheric model for climate prediction*. arXiv. Retrieved 2024-05-17, from <http://arxiv.org/abs/2310.02074> (arXiv:2310.02074) doi: 10.48550/arXiv.2310.02074

Watt-Meyer, O., Henn, B., McGibbon, J., Clark, S. K., Kwa, A., Perkins, W. A., ... Bretherton, C. S. (2024). *ACE2: Accurately learning subseasonal to decadal atmospheric variability and forced responses* (No. arXiv:2411.11268). arXiv. Retrieved 2024-11-25, from <http://arxiv.org/abs/2411.11268> doi: 10.48550/arXiv.2411.11268

Weyn, J. A., Durran, D. R., & Caruana, R. (2020). Improving Data-Driven Global Weather Prediction Using Deep Convolutional Neural Networks on a Cubed Sphere. *Journal of Advances in Modeling Earth Systems*, 12(9), e2020MS002109. Retrieved 2024-02-12, from <https://onlinelibrary.wiley.com/doi/abs/10.1029/2020MS002109> doi: 10.1029/2020MS002109

Weyn, J. A., Durran, D. R., Caruana, R., & Cresswell-Clay, N. (2021). Sub-Seasonal Forecasting With a Large Ensemble of Deep-Learning Weather Prediction Models. *Journal of Advances in Modeling Earth Systems*, 13(7), e2021MS002502. Retrieved 2024-05-14, from <https://onlinelibrary.wiley.com/doi/abs/10.1029/2021MS002502> doi: 10.1029/2021MS002502

Whan, K., Zwiers, F., & Sillmann, J. (2016, June). The Influence of Atmospheric Blocking on Extreme Winter Minimum Temperatures in North America. *Journal of Climate*, 29(12), 4361–4381. doi: 10.1175/JCLI-D-15-0493.1

Woollings, T. (2010). Dynamical influences on European climate: an uncertain future. *Philosophical Transactions: Mathematical, Physical and Engineering Sciences*, 368(1924), 3733–3756. Retrieved 2024-05-21, from <https://www.jstor.org/stable/25699197>

Woollings, T., Gregory, J. M., Pinto, J. G., Reyers, M., & Brayshaw, D. J. (2012). Response of the north atlantic storm track to climate change shaped by ocean–atmosphere coupling. *Nature Geoscience*, 5(5), 313–317. Retrieved 2025-02-05, from <https://www.nature.com/articles/ngeo1438> (Publisher: Nature Publishing Group) doi: 10.1038/ngeo1438

Young, A. H., Knapp, K. R., Inamdar, A., Hankins, W., & Rossow, W. B. (2018). The International Satellite Cloud Climatology Project H-Series climate data record product. *Earth System Science Data*, 10(1), 583–593. Retrieved 2024-05-09, from <https://essd.copernicus.org/articles/10/583/2018/> doi: 10.5194/essd-10-583-2018[Dataset]

Zarzycki, C. M., & Ullrich, P. A. (2017). Assessing sensitivities in algorithmic detection of tropical cyclones in climate data. *Geophysical Research Letters*, 44(2), 1141–1149. doi: <https://doi.org/10.1002/2016GL071606>

Zonca, A., Singer, L. P., Lenz, D., Reinecke, M., Rosset, C., Hivon, E., & Gorski, K. M. (2019). healpy: equal area pixelization and spherical harmonics transforms for data on the sphere in Python. *Journal of Open Source Software*, 4(35), 1298. Retrieved 2024-08-05, from [https://joss.theoj.org/papers/4\(35\), 1298](https://joss.theoj.org/papers/4(35), 1298)

10.21105/joss.01298 doi: 10.21105/joss.01298[Software]

Supporting Information for

## A Deep Learning Earth System Model for Efficient Simulation of the Observed Climate

Nathaniel Cresswell-Clay<sup>1</sup>, Bowen Liu<sup>1,2</sup>, Dale R. Durran<sup>1</sup>, Zihui Liu<sup>1</sup>,  
Zachary I. Espinosa<sup>1</sup>, Raul A. Moreno<sup>1</sup>, Matthias Karlbauer<sup>3</sup>

<sup>1</sup>University of Washington  
<sup>2</sup>Institute of Atmospheric Physics, CAS  
<sup>3</sup>University of Tübingen

### Contents of this file

Text S1 to S5  
Figures S1 to S4  
Table S1

### Additional Supporting Information (Files uploaded separately)

None

### Introduction

Supporting information for the manuscript entitled “A Deep Learning Earth System Model for Efficient Simulation of the Observed Climate” is contained in this compiled PDF file. There are no externally uploaded materials. Within this PDF, we include several sections of text that offer important details which will be relevant to interested experts, but is not essential for understanding the conclusions of the study. This file contains figures and a table that are used to present these details.

## S1 Component Model Details

### S1.1 Deep Learning Weather Prediction Model

The DLWP training dataset is made up of four types of input: the 9 prognostic fields predicted by DLWP as well as 2 constant fields, 1 prescribed field, and 1 coupled field. Each of these inputs is interpreted by the neural net as a single channel. The constant fields are topographic height and land-sea fraction; the prescribed field is  $I_{TOA}$  (which is calculated as a function of time, longitude, and latitude); the coupled field is SST. DLWP is trained on 33 years of observations (1983-2016) and validated on 1 year of observations (2016-2017).

As in (Weyn et al., 2020), the atmosphere model is trained to optimize global root mean squared error (RMSE) over 24 hours from 6-hourly data generated by two successive model steps. Choosing a 24-h period for the loss allows the model to learn the atmospheric evolution in a complete diurnal cycle over the full globe without pushing it toward a multi-day ensemble-mean forecast. Despite removing appropriate global mean values, and normalizing all the prognostic variables by their standard deviation, the contributions to the loss among individual variables differ by orders of magnitude; OLR and TCWV generate the largest losses, while  $Z_{250}$  produces the smallest. We scale the weight for the  $i^{\text{th}}$  variable,  $w_i$ , to ensure the contributions to the RMSE loss function from each variable have similar magnitude by setting  $w_i = 0.001/V_i$ , where  $V_i$  is the unscaled validation loss for the  $i^{\text{th}}$  variable after a 10-epoch training. Improvements achieved from this weighting are not sensitive to the exact values of  $w_i$ .

Here we note some important hyperparameter choices; the full model configuration appears in the code repository associated with this article. Throughout training, we use the cosine annealing leaning rate scheduler as formulated by PyTorch’s `optim` library (Paszke et al., 2019) over our 250 epoch training cycle. We used gradient clipping with `max_norm=0.25`. The DLWP model training took roughly 4.5 days on 4 NVIDIA A100 80GB graphics processing units (GPUs).

### S1.2 Deep Learning Ocean Model

Like DLWP, DLOM also has four basic types of input: prognostic, constant, prescribed, and coupled. SST is the single prognostic field predicted by our ocean component; DLOM receives  $F_{LS}$  as a constant field;  $I_{TOA}$  as a prescribed field; and  $WS_{10m}$ ,  $Z_{1000}$  and OLR from the atmosphere. The coupled fields used to force the training of the DLOM component have been averaged over times  $t_0-t_{48}$  and  $t_{48}-t_{96}$ . This treatment of the incoming atmospheric fields is designed to mimic the behavior during inference (Section 2.2). Notably, we do not use  $T_{2m}$  as a forcing field for DLOM, despite it being a prognostic field of our DLWP model. This is done to avoid SST values matching the  $T_{2m}$  field above the ocean, when in fact it is the SST that should determine  $T_{2m}$  over the ocean.

The DLOM component model is trained to optimize maritime RMSE over 192 h of prediction. Maritime RMSE is defined as the RMSE spatially weighted by  $1-F_{LS}$ . DLOM has 48-h resolution and so we advance 192 h from two auto-regressive calls (similar to the two calls in DLWP training).

Training DLOM models is more sensitive than training DLWP models. To achieve best results, we employed a staged learning program with 3 phases. The program proceeded for 300 epochs, with a cosine annealing restart every 100 epochs using the best checkpoint from the previous phase. Maximum (minimum) learning rates for each phase were 1e-4 (4e-5), 5e-5 (5e-6) and 2.5e-5 (0), respectively.

Variable Name	Symbol	Source	Preprocessing
1000-hPa geopotential height	$Z_{1000}$	ERA5	-
500-hPa geopotential height	$Z_{500}$	ERA5	-
250-hPa geopotential height	$Z_{250}$	ERA5	-
700–300-hPa thickness	$\tau_{300-700}$	ERA5	difference between 300 and 700-hPa geopotential heights
2-m temperature	$T_{2m}$	ERA5	-
850-hPa temperature	$T_{850}$	ERA5	-
total column water vapor	TCWV	ERA5	-
10-m windspeed	$WS_{10}$	ERA5	magnitude of 10-m horizontal velocity vector
sea surface temperature	SST	ERA5	land imputation
outgoing longwave radiation	OLR	ISCCP	brightness conversion and OLR imputation
land-sea fraction	$F_{ls}$	ERA5	-
surface elevation	$z$	ERA5	-
top of atmosphere insolation	$I_{TOA}$	-	-

**Table S1. Initialization fields Earth System fields for DLESyM.** The columns show the variable name, the abbreviated symbol for the variable, the data source, extra preprocessing steps used to prepare data for training/inference

### S1.3 Deep Learning Precipitation Diagnosis

The input to the diagnostic precipitation module is the same two-time-level tensor of prognostic, constant, and prescribed variables as DLWP, but rather than a recurrent forecast, its output  $P$  is the cumulative 6-h precipitation between the two sequential times. The ERA5 precipitation over the same period is the target. Because precipitation is highly skewed, the loss function is evaluated as in (Rasp & Thuerey, 2021) using the log-transformed field

$$\tilde{P} = \ln(1 + P/\epsilon)$$

where  $\epsilon = 1 \times 10^{-8}$  m. To emphasize heavy precipitation events, the cost function,  $L$ , for our precipitation module is the global RMSE scaled by the exponentially transformed field,

$$L = \exp(b * \tilde{P}) \times RMSE$$

where  $b = 0.4$  is a tuned hyperparameter.

## S2 Data Sources

### S2.1 ERA5

ECMWF reanalysis version 5 (ERA5) (Hersbach et al., 2020) is the primary dataset used for training and verification of DLESyM, providing these prognostic fields: geopotential at 1000, 700, 500, 300 and 250 hPa, temperature at 2-m and 850 hPa, total column water vapor, and SST. We also use two ERA5 time-invariant fields for training and inference: terrain height and land-sea fraction (called surface geopotential and land-sea mask in ERA5 database respectively). Some of these fields require additional preprocessing using other ERA5 fields as indicated in Table S1. DLESyM discretizes all fields using the Hierarchical Equal Area isoLatitude Pixelization (HEALPix) (Górski et al., 2005; Karlbauer et al., 2024; Zonca et al., 2019), with the 12 primary HEALPix faces divided into  $64 \times 64$  cells, giving a total of 49,152 cells globally. The diagonal distance between

adjacent cell centers is approximately 110 km, which in turn is approximately  $1^\circ$  of latitude at the equator.

As part of this reprocessing, SST values over the continents are imputed using zonal linear interpolation. This coast-to-coast interpolation ensures that our convolutional operations yield reasonable values throughout our domain while minimizing the sharp gradients near the land-sea boundaries. As a possible alternative to zonally interpolated imputation, we also tested the using zonal climatological averages for SSTs over land, but this tended to produce nonphysical features in the ocean state during long rollouts. Although the full global SST is updated every step, the values over land are masked and ignored in the loss function during training.

## S2.2 ISCCP

The International Satellite Cloud Climatology Project (ISCCP) calibrates and compiles observations from a large suite of satellites into a single dataset (Young et al., 2018). Here we use the "IR Brightness Temperature" from the HXG distribution, which is available from 1983 to 2017 at 3-hour resolution on a 0.1 degree latitude-longitude mesh. The ISCCP data requires several preprocessing steps before it is ready for training. There are swaths of missing data, notably prior to 1998 over the Indian Ocean, which are filled in using ERA5's model-derived total net thermal radiation (TTR) field. To complete this imputation, IR brightness temperature is converted to outgoing longwave radiation (OLR), in units of  $\text{W m}^{-2}$ , by the Stefan–Boltzmann law, and downsampled from the 0.1 degree latitude-longitude mesh to a  $0.25^\circ$  mesh to match the ERA5 grid. Then TTR, in units of  $\text{J m}^{-2}$ , is scaled to match the distribution of the ISCCP brightness temperatures using the relation:

$$\widehat{\text{TTR}} = \frac{\sigma_{\text{OLR}}}{\sigma_{\text{TTR}}} (\text{TTR} - \mu_{\text{TTR}}) + \mu_{\text{OLR}} \quad (1)$$

where  $\widehat{\text{TTR}}$  is scaled TTR,  $\sigma_{\text{OLR}}$  is the standard deviation of the outgoing longwave radiation,  $\sigma_{\text{TTR}}$  is the standard deviation of the TTR,  $\mu_{\text{TTR}}$  is the mean TTR, and  $\mu_{\text{OLR}}$  is the mean outgoing longwave radiation. Once scaled, we use the TTR to impute the outgoing longwave radiation over the missing regions of missing ISCCP data. A 2D Gaussian filter is used to smooth seams in the ISCCP observations and the imputed TTR. The result is a realistic OLR record that contains no missing data. Like ERA5 sourced data, ISCCP data was mapped onto the HEALPix mesh for training and inference.

## S3 Tropical Cyclone Detection

Following (Ullrich et al., 2021; Zarzycki & Ullrich, 2017), this study categorizes tropical cyclones into four groups based on these three criteria:

1. The local minimum in SLP drops below predefined thresholds within the western North Pacific region ( $100^\circ\text{E}$ – $160^\circ\text{E}$ ,  $5^\circ\text{N}$ – $35^\circ\text{N}$ ). These thresholds are round numbers approximating the 1st, 0.1st, 0.01st, and 0.001st percentile SLP values. For SLP fields sampled once per day these values are 1000, 994, 985, 975 hPa.
2. The presence of a well-defined upper-level warm core. A warm core is defined as the geopotential layer thickness between 300 and 700 hPa that exceeds the seasonally varying climatological value.
3. The tropical cyclone trajectories are continuous. The adjacent centers along the same track are separated by no more than 2 days in time and 3 degrees in spatial distance. Tracks containing fewer than 3 data points are not considered in the analysis. Tropical cyclone tracks from ERA5 and DLESyM are compared in Fig. 5.

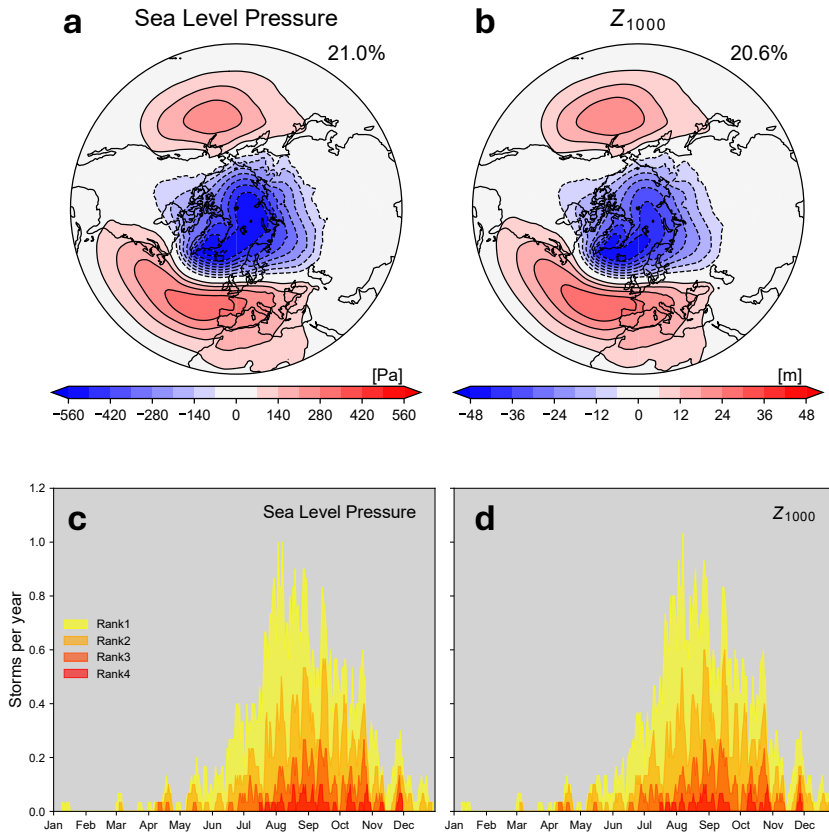


**Figure S1. Correspondence between sea level pressure (SLP) and  $Z_{1000}$  in TC and NAM analyses.** Leading mode of NH variability in ERA5 evaluated using (a) SLP and (b)  $Z_{1000}$ . Calculated over 40 years of ERA5 record (1970-2010). Contour intervals in Pa and m, as labeled, to reveal the same pattern. TC detection algorithm applied to ERA5 using (c) SLP and (d)  $Z_{1000}$ . Nearly identical structure of TC frequency using the rank 1 to rank 4 thresholds noted in Supporting Information Section S3 justifies comparisons between DLESyM simulations (which only predict  $Z_{1000}$ ) and CMIP6 output (which only reports SLP).

The DLESyM analysis employed  $Z_{1000}$  to identify tropical cyclones because it does not include SLP in its state vector. Both variables are available in ERA5, which allows us to calibrate the  $Z_{1000}$  values in the DLESyM rollout for comparison with the CMIP6 historical runs. The difference between using SLP and  $Z_{1000}$  for detecting tropical cyclones, with appropriately scaled thresholds, was negligible. Choosing 0, -50, -130, -230 m as the  $Z_{1000}$  thresholds corresponding to those previously noted for SLP, we obtain essentially the same distribution as using SLP (Fig. S1c,d). The correlations between the distributions for Ranks 1 to 4 is 0.99, 0.99, 0.98, and 0.89, respectively.

#### S4 Annular Mode Computation

The CMIP6 models used in this study do not have complete  $Z_{1000}$  fields, and so we utilized sea-level pressure (SLP), a field not available in the DLESyM, to calculate the NAM for the CMIP6 models. The spatial correlation between the ERA5 NAM computed from the  $Z_{1000}$  and the SLP fields is 0.99, and, when plotted with properly calibrated contour intervals, their signatures are essentially identical. Using these contour intervals for intercomparison in Fig. 8a–f, the NAM is plotted based on the  $Z_{1000}$  field for ERA5 and the DLESyM rollout while the NAM is calculated from SLP for the CMIP6 historical runs. To maximize compatibility, the statistics for the NAM calculated from CMIP6 data are compared against the ERA5 SLP record in the Taylor diagrams in Fig. 7.

The correlation between the NAM (SAM) index in this paper and the identical but alternatively named Arctic Oscillation (Antarctic Oscillation) index in daily time series provided by the Climate Prediction Center (CPC; <https://www.cpc.ncep.noaa.gov/>) for 1970–2010 (1979–2010) is 0.98 (0.93).

#### S5 Indian Summer Monsoon

Analyses reporting the Indian Summer Monsoon or ISM follow metrics defined in (B. Wang & Fan, 1999). Outgoing longwave radiation values are spatially averaged between 10° and 25° North and 70° and 100° East to obtain the ISM index. Plotted time series in Fig. 9a are daily average values of this ISM Index.

Here we examine DLESyM’s treatment of monsoon onset during May and June in a 6-month forecast beginning on January 1, 2017. 2-week averaged fields of OLR and 2-week accumulated precipitation are plotted in Figs. S2 and S3, respectively. The OLR is observed by satellite, while the ERA5 precipitation in this region is generated by the ECMWF’s global forecast model during each reanalysis cycle. Considering the six-month forecast lead time, the predicted and analyzed fields are in reasonably good agreement in three of the four 2-week periods, with substantial differences only during May 15–28.

The climatological monsoon cycle has large amplitude. Indeed DLESyM’s ability to capture this climatological evolution (Fig. S4) contributes to its apparent skill over the seasonal forecast. The extent to which DLESyM can correctly capture interannual variations in monsoon onset in ensemble forecasts is a subject of current research. Nevertheless, Figs. S2 and S3 demonstrate that key atmospheric fields simulated by DLESyM at the end of the 6-month rollout are physically realistic.

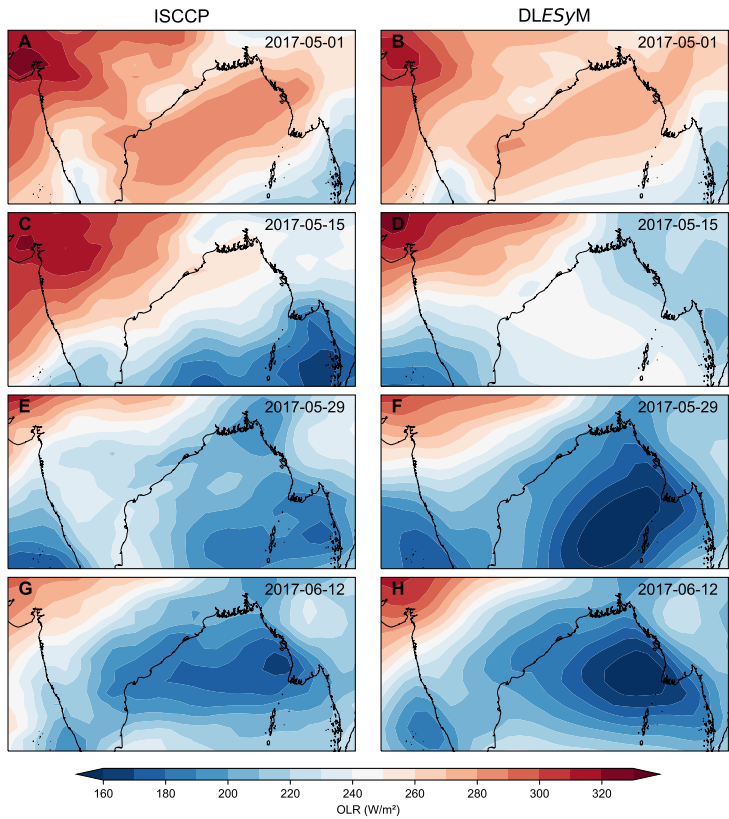


**Figure S2. Extended ISM OLR forecast with DLESyM.** May–June 2017 progression of 2-week-averaged OLR for the period beginning on the date noted in each panel in (A), (C), (E), (G): ISCCP data, and (B), (D), (F), (H): 6-month DLESyM forecast from January 1, 2017.

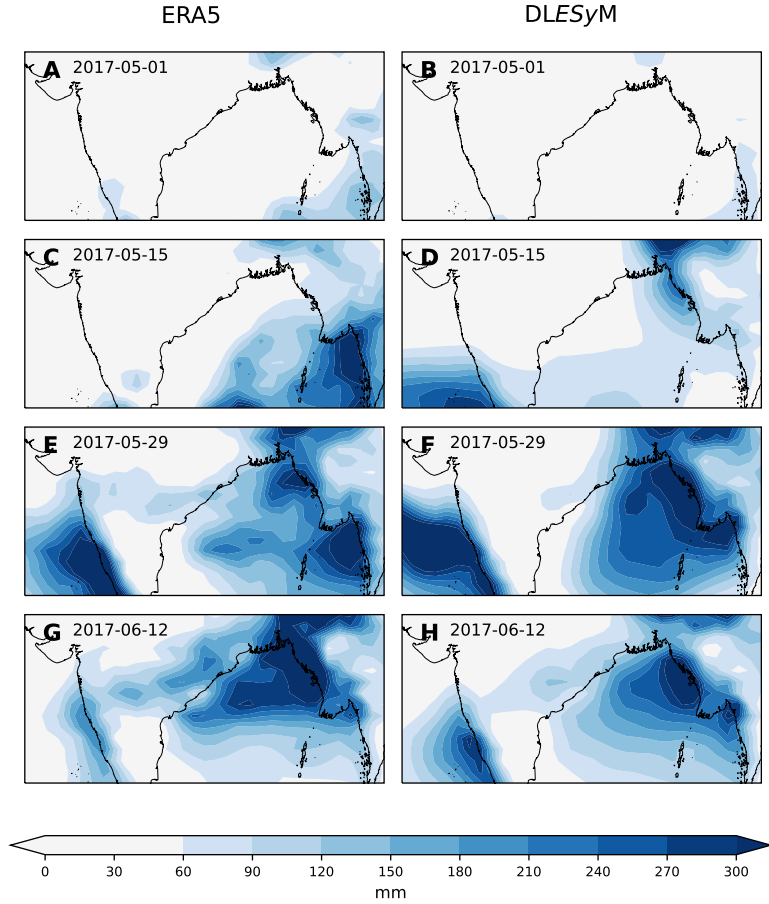


**Figure S3. Extended ISM precipitation forecast with DLESyM.** May–June 2017 progression of 2-week accumulated precipitation fields for the period beginning on the date noted in each panel in (A), (C), (E), (G): ERA5, and (B), (D), (F), (H): 6-month DLESyM forecast from January 1, 2017. Considering the six-month forecast lead time, the predicted and analyzed fields are in reasonably good agreement in three of the four 2-week periods, with substantial differences only during May 15–28.

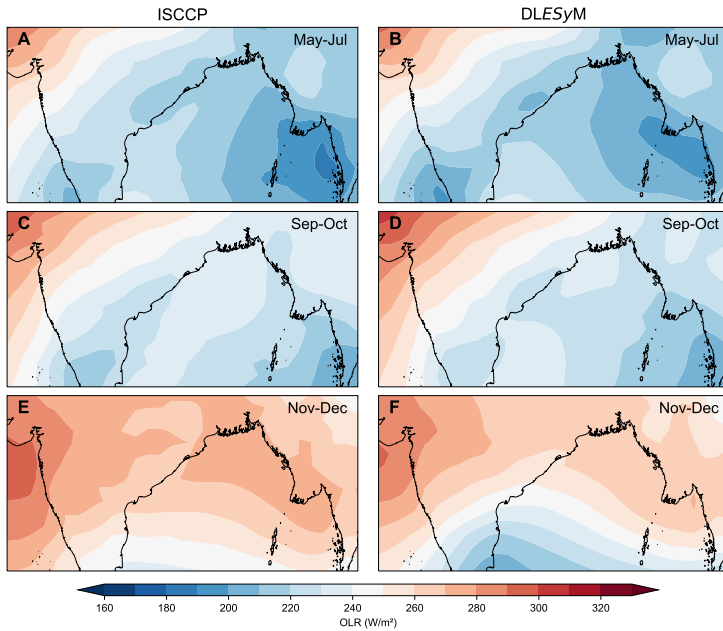


**Figure S4. Climatological evolution of Indian Summer Monsoon (ISM) OLR in 100-year DLESyM simulation.** Annual cycle of multi-month averaged of OLR in (A), (C), (E) ISCCP data for 1985-2014, and (B), (D), (F) years 2085-2114 in the DLESyM rollout. Averaging period is indicated in each panel. During monsoon onset (May–July) and the beginning of its southward retreat (September–October), the DLESyM fields are in close agreement with the observations. In the November–December period, however, the OLR values are too low over southern India and the adjacent Indian Ocean, which leads to the errors at low-latitudes apparent in November and December in Fig. 9a,e.